Check for updates

Advanced Energy Materials

SPECIAL ISSUE Advances and Challenges in Sodium-Ion Battery Technology

ADVANCED ENERGY MATERIALS
www.advenergymat.de

RESEARCH ARTICLE OPEN ACCESS

Prediction of Structural Stability of Layered Oxide Cathode Materials: Combination of Machine Learning and Ab Initio Thermodynamics

Liang-Ting Wu[1,2,3] | Milica Zdravković[1,4] | Dijana Milosavljević[1] | Konstantin Köster[1,4] | Olivier Guillon[1] | Jyh-Chiang Jiang[2,3] | Payam Kaghazchi[1,4]

[1]Materials Synthesis and Processing (IMD-2), Institute of Energy Materials and Devices, Forschungszentrum Jülich GmbH, Jülich, Germany | [2]Department of Chemical Engineering, National Taiwan University of Science and Technology, Taipei, Taiwan | [3]Sustainable Electrochemical Energy Development (SEED) Center, National Taiwan University of Science and Technology, Taipei, Taiwan | [4]MESA+ Institute, University of Twente, Enschede, NH, The Netherlands

Correspondence: Payam Kaghazchi (p.kaghazchi@fz-juelich.de)

Received: 26 September 2025 | **Revised:** 26 November 2025 | **Accepted:** 27 November 2025

Keywords: first principles | layered oxide materials | machine learning | Na-ion batteries | phase stability

ABSTRACT

Layered oxides have caught much attention as cathode materials for Na-ion batteries. For a rational cathode material design and performance improvement, accurate prediction of the most stable stacking sequence (e.g., P2 vs. O3 phase) of layered oxides is inevitable. Here, we first developed a data-driven model based on machine learning (ML) to predict the phase stability of layered oxides. Afterward, with combination of electrostatic analysis, density functional theory, Monte Carlo simulation, and thermodynamics consideration, we validated our ML-based prediction and gained insight into the interrelation between features and phase stabilities. We found that deep neural networks can predict phase stability with a very high accuracy. TM ionic potential, Na concentration, and TM mixing entropy are identified as the key factors influencing phase classification, with lower TM ionic potential, higher Na content, and higher mixing entropy favoring the O3 phase. We found that Na-TM and Na-Na interactions are key factors controlling the phase stability and both are strongly Na concentration dependent. Finally, the TM ionic potential is determined to be the decisive factor controlling Na-TM interaction and thereby the phase stability of layered oxide cathode materials for Na-ion batteries.

1 | Introduction

The world has a continuous need for energy storage in the form of batteries that can integrate well with renewable energy sources [1–4]. Lithium-ion Batteries (LIBs) dominate the mobile energy storage market and are considered the most favored option for electric vehicles. However, the mass production of LIBs will face challenges such as the price of Li as well as the cost and environmental impact of transition metals (TMs), which are needed for the cathode materials in the near future. Therefore, a large portion of research is concentrated on the development of sodium-ion batteries (SIBs), as Na is extremely abundant and cheap, and TMs which are used in cathode side can be more affordable and less critical [5]. Layered oxide materials are the most promising cathodes for SIBs, but certain design challenges must be overcome to achieve capacity and charge-discharge cycle stability that is competitive to that of LIBs. Li and Na layered oxides can crystallize in various different stacking structures or crystallographic phases [6]. However, while Li layered oxides are generally found in the octahedral (O-type) configuration, Na layered oxides (Na_xTMO_2) can occur both in the O-type and prismatic (P-type) phases, the latter being more common [6, 7].

This is an open access article under the terms of the Creative Commons Attribution License, which permits use, distribution and reproduction in any medium, provided the original work is properly cited.

© 2025 The Author(s). *Advanced Energy Materials* published by Wiley-VCH GmbH

Evidence suggests that P2 structures have better Na-ion conductivity [8], but they typically contain lower initial Na than O3 structures, which can reduce the initial capacity [9]. Therefore, a method of phase prediction can facilitate the rational design of Na_xTMO_2 cathode materials. Zhao et al. proposed a methods in Ref. [7], wherein the authors define the cationic potential (ϕ_{cation}) and demonstrate how it can accurately classify materials into O3 and P2 structure types. The cationic potential is the product of the mean TM and Na ionic potentials, normalized to the ionic potential of O. Here, the ionic potentials (ϕ) is defined as the ratio of the charge (q) to the ionic radius (r), reflecting the polarizing power of the ion [10]. The aforementioned study calculated the cationic potential for 104 different types of Na_xTMO_2 cathode materials and found that O3 structures had a higher Na-ionic to cationic potential ratio than P2 structures. The prediction method is analogous to that of a linear classifier in machine learning. Since the development of this method in 2020, cationic potential has been used as the primary predictor of phase when designing Na_xTMO_2 cathode materials. However, by definition, the cationic potential implicitly contains several more parameters (Na content, TM ionic radius, and TM charge).

Machine learning (ML) can provide insights into chemical and physical properties hidden within numerous experimental and computational datasets and accelerate material development [11]. ML has, for example, been widely used in atomistic property prediction [12–14] as well as interatomic potential training [15, 16] and molecular structure optimization [17, 18]. Another well-known example is the discovery of AlphaFold 3 model that has significantly advanced our understanding of protein folding and protein–protein interactions and, consequently, was awarded the Nobel Prize in Chemistry in 2024 [19–21]. Moreover, various regression, clustering, and classification ML models are widely used in data-driven energy storage material development. For instance, Austin et al. used a logistic regression model to identify fast lithium conductors based on experimental measurements and to distinguish between superionic structures ($\sigma \geq 10^{-4}$ S cm^{-1}) and non-superionic structures ($\sigma < 10^{-4}$ S cm^{-1}) [22]. Rajendra et al. employed deep neural network models to predict the voltage of electrode materials in a given metal-ion battery [23]. Kristen et al. predicted the cycle life of commercial lithium iron phosphate (LFP)/graphite cells based on early-cycle data via elastic net–regularized regression [24]. In the area of materials science state-of-the-art techniques include graph neural networks (GNNs) such as atomistic line graph neural networks (ALIGNN) [25] and Crystal Hamiltonian Graph Neural Network (CHGNet) [16], that were shown to be capable of predicting several properties including energies and forces from a given materials geometry.

Our previous work demonstrated that predicting molecular properties (solvent–ion interaction) is efficient via multiple linear regression (MLR) by selecting features with relevant physical/chemical meaning (charge density), even for a small dataset [26]. For the specific task of binary classification, logistic regression (LR) [27], support vector machines (SVMs) [28], naive Bayes (NB) [29], random forest (RF) [30], k-nearest neighbors (k-NN) [31], and deep neural networks (DNNs) are among the most commonly applied. LR is a statistical method that utilizes the logistic (a type of sigmoid) function to convert a linear combination of inputs into probabilities [27, 32]. SVMs find an optimal decision boundary by maximizing the margin between classes [28] and NB use Bayes' theorem to estimate class probabilities [29]. RF is an ensemble method that combines multiple decision trees to improve accuracy and reduce overfitting, making it suitable for both classification and regression tasks [30] while k-NN is a non-parametric method that classifies data points based on the majority class of their nearest neighbors [31]. DNNs utilize multiple layers to learn complex features, requiring large datasets and substantial computational power [33]. First principles approaches such as electrostatic and density functional theory (DFT) are valuable tools to compute electronic and atomistic structures as well as formation energy [34–37]. A combination of ML and first principles calculation can be applied to predict the phase stability and understand key features controlling this property.

In this work, we present a ML-predictor as well as ab initio, statistical, and thermodynamics methods which can help a rational design of layered oxide cathode materials for SIBs. Various ML models were first trained using the experimental data of 270 different sodium-layered cathode materials. We extended the input parameter space to a total of 6 parameters: ionic potential of TM, Na concentration, TM mixing entropy, cationic potential, TM ionization energy, and TM radius. We also evaluated Shapley additive explanations (SHAP) and the permutation importance of each feature, exploring how the features affect the preferred phase (P2 or O3) of layered cathode materials. Afterward, we quantified phase stability and determined key parameters controlling this property for selected compounds (from the ML-prediction) using electrostatic and DFT calculation together with Monte Carlo simulation and thermodynamic approaches. This work can enhance our understanding of SIB layered oxide cathode materials and provides an efficient tool for predicting their most stable phase.

2 | Methodology

2.1 | Features Selection

The ionic potentials of Na and O were calculated using Equation 1. For the features related to TMs, values were weighted by the concentration of each TM. Specifically, the TM concentration (n_{TM}), TM radius (r_{TM}), TM charge (q_{TM}), TM ionic potential (ϕ_{TM}), and TM ionization energy (I_{TM}) were calculated using Equations 2–6. The cationic potential was determined using Equation 7 [7], while the TM mixing entropy was computed using Equation 8.

$$\phi_i = \frac{q_i}{r_i} \tag{1}$$

$$n_{TM} = \sum_j n_j \tag{2}$$

$$r_{TM} = \frac{\sum_j n_j r_j}{n_{TM}} \tag{3}$$

$$q_{TM} = \sum_j n_j q_j \tag{4}$$

$$\phi_{TM} = \sum_j n_j \frac{q_j}{r_j} \tag{5}$$

16146840, 2026, 42, Downloaded from https://advanced.onlinelibrary.wiley.com/doi/10.1002/aenm.202505470 by Forschungszentrum Juelich GmbH, Wiley Online Library on [17/11/2026]. See the Terms and Conditions (https://onlinelibrary.wiley.com/terms-and-conditions) on Wiley Online Library for rules of use; OA articles are governed by the applicable Creative Commons License

$$I_{TM} = \sum_j n_j I_j \tag{6}$$

$$\phi_{cation} = \frac{\phi_{Na}\phi_{TM}}{\phi_O} \tag{7}$$

$$S_{TM} = -\sum_j n_j \ln\left(n_j\right) \tag{8}$$

where q_i and n_i represent the charge and concentration of element i (for i = Na, O). The variables n_j, r_j, q_j, and I_j denoted the concentration, radius, charge, and ionization energy for element j located in the TMO_2 layer, even if the element is not strictly a TM (e.g., Li, Mg, etc.). These properties are dependent on the oxidation state.

The charge of each element was calculated to ensure charge balance. Elements with only one possible oxidation state had their charges directly assigned to their oxidation states (e.g., Na (+1), Li (+1), Mg (+2), etc.). For elements with multiple oxidation states, the charge was initially assigned as +3. The charges are then adjusted if excess positive or negative charges exist in the material. The element with lower (higher) electronegativity will be partially or fully oxidized (reduced) first until the material reaches charge neutrality. The detailed algorithm is provided in the code available online: https://github.com/LIANGTING-WU/ML_Phase_Predictor.

2.2 | Evaluation Metrics

The confusion matrix of the binary classification was used to evaluate the models [38], monitoring four metrics, accuracy, precision, recall, and F1 score, defined by the following equations:

$$Accuracy = \frac{\text{True O3} + \text{True P2}}{\text{True O3} + \text{True P2} + \text{False O3} + \text{False P2}} \tag{9}$$

$$Precision = \frac{\text{True O3}}{\text{True O3} + \text{False O3}} \tag{10}$$

$$Recall = \frac{\text{True O3}}{\text{True O3} + \text{False P2}} \tag{11}$$

$$F1\,Score = 2 \times \frac{Recall \times Precision}{Recall + Precision} \tag{12}$$

where True O3 is the number of compositions that are actually O3-type and correctly predicted as O3-type; True P2 is the number of compositions that are actually P2-type and correctly predicted as P2-type; False O3 is the number of compositions that are actually P2-type but were misclassified by the tested model as O3-type; and False P2 is the number of compositions that are actually O3-type but were misclassified as P2-type.

2.3 | Machine Learning Models

Implementations of LR, SVM, NB, RF, and k-NN are provided by scikit-learn [39], a Python-based machine learning library. All features were standardized by subtracting their mean values and dividing by their standard deviations

$$z = \frac{x - \mu}{\sigma} \tag{13}$$

where x is the original feature, and μ and σ are the calculated mean and standard deviation over all compositions, respectively.

To mitigate overfitting, we employed tenfold cross-validation (CV) [26] for the LR, SVM, NB, and k-NN models, assigning 10% of the data as a test set and 90% for training in each fold. For hyperparameter tuning in the LR and SVM models, we sampled candidate values on a logarithmic scale to cover a wide range of magnitudes. The LR model's hyperparameter, the inverse regularization strength, was tested at values of 0.001, 0.005, 0.01, 0.02, 0.05, 0.1, 0.5, 1, and 10. The value of 0.05 was found to be optimal. For SVM, we used a linear kernel and tested the penalty parameter at 0.001, 0.005, 0.01, 0.02, 0.05, 0.1, 0.5, 1, 5, 10, 50, 100, 500, and 1000. The optimal parameter was determined to be 100. Since the features are continuous, Gaussian Naive Bayes was employed for NB. The number of estimators in the RF model was tested at 1, 2, 3, 4, 5, 10, 20, 50, 100, 200, and 500.5 was chosen because the F1 score converged after 5. For the k-NN model, the numbers of neighbors tested were 1, 3, 5, 7, 9, and 11, and k = 5 yielded the highest performance. Throughout hyperparameter optimization, the F1 score was used as the selection criterion and corresponding optimization plots are shown in supporting information (Figures S4–S7).

The DNN model was constructed using the TensorFlow library [40], with 12, 8, 6, and 3 neurons in the first, second, third, and fourth hidden layer, respectively. The rectified linear unit (ReLU) activation function was used, as shown in Equation 14 [41], and a sigmoid activation function (Eq. 15) [42] was applied in the output layer for the binary classification task. The loss function was defined by binary cross-entropy (Eq. 16) [43]. To enhance model generalization and speed up training, we employed Kaiming initialization [44], batch normalization [45], and dropout [46]. We also used an exponential decay schedule (Eq. 17) for the learning rate [47], starting at 0.012 with a decay rate of 0.9 every 70 steps.

$$\text{ReLU}\ (x) = \max\left(0, x\right) \tag{14}$$

$$\text{Sigmoid}\ (x) = \frac{1}{1 + e^{-x}} \tag{15}$$

$$L = -\frac{1}{N}\sum_{i=1}^{N}\left[y_i \ln\left(\hat{y}_i\right) + \left(1 - y_i\right)\ln\left(1 - \hat{y}_i\right)\right] \tag{16}$$

$$\alpha\left(t\right) = \alpha_0 r^{-\frac{t}{s}} \tag{17}$$

In the equations above, L represents the loss function, y_i is the actual label of each composition (0 for P2 or 1 for O3), $\hat{y}_i$ is the probability that the model classifies the composition as O3-type, and N is the number of samples. In the exponential decay schedule, $\alpha(t)$ and α_0 are the epoch-dependent and initial learning rates, respectively, r is the decay rate, s is the decay step, and t is the current epoch.

16146840, 2026, 42, Downloaded from https://advanced.onlinelibrary.wiley.com/doi/10.1002/aenm.202505470 by Forschungszentrum Juelich Gmbh, Wiley Online Library on [17/11/2026]. See the Terms and Conditions (https://onlinelibrary.wiley.com/terms-and-conditions) on Wiley Online Library for rules of use; OA articles are governed by the applicable Creative Commons License

2.4 | Features Analysis

We calculated the permutation importance of each feature for every model by randomly shuffling the feature values and monitoring the resulting drop in model performance (here, measured by the F1 score) [48]. The feature was shuffled 50 times, and the importance was determined using scikit-learn's built-in functionality. Additionally, we employed the Shapley additive explanations (SHAP) method to explain the model outputs based on Shapley values. The SHAP analysis was conducted for the DNN model using the SHAP Python package [49]. SHAP values for each feature shift the raw logits with respect to the baseline, and the SHAP value for each feature is additive for each data point. Therefore, the model output is determined by the sum of the SHAP values for all features, as shown in Equation 18:

$$f\ (x) = \psi_0 + \sum_i \psi_i \tag{18}$$

where $f(x)$ represents the model output before passing through the sigmoid function (i.e., the output in the raw logit space); ψ_0 represents the baseline model output; and ψ_i represents the SHAP value for feature i. Positive (negative) SHAP values increase (decrease) the output in the raw logit space and thereby raise (reduce) the probability of being classified into the O3-type class for a specific composition.

2.5 | Atomistic Structure Models and Electrostatic Calculation

To model the selected compositions, the first step is to obtain the lowest energy arrangement of Na and TM ions in the lattice sites. By calculating the Coulomb energies of possible configurations, we identify global minimum energy structures. A $(2\sqrt{3}) \times (2\sqrt{3}) \times 1$ supercell was employed to model the structures. The P2 supercell comprises a total of 24 TM atoms, whereas the O3 cell contains 36 TM atoms. We constructed all possible atomistic arrangements and calculated the global energy minimum in these structures using the Electrostatics optimization software GOAC [50]. A custom script, developed based on Pymatgen package [51] was employed to calculate individual pairwise electrostatic interactions.

2.6 | Entropy

Mixing entropy (Equation 8) on its own does not represent thermodynamic entropy. However, it is proportional to the Entropy of Mixing for ideal gases, given by [52]:

$$\begin{aligned} S_{Mix} &= -\mathrm{k_B} N \sum_i x_i \ln(x_i) \\ &= -\mathrm{k_B} N S_{TM} \end{aligned} \tag{19}$$

where $\mathrm{k_B}$ is the Boltzmann constant, N is the total number of particles being mixed (in this case, the number of TMs), and x_i is the concentration of the individual TM atoms in the chemical formula. In practice however, the cathode material in this study are not gas mixtures but layered oxide crystal, with fewer degrees of freedom, and so the true entropy should be lower than S_{Mix}. We can calculate the entropy using the Gibbs entropy formula:

$$S = -\mathrm{k_B} \sum_i p_i \ln(p_i) \tag{20}$$

where p_i is the probability of microstate i. In the case of configurational entropy, a microstate refers to one possible atomistic configuration for the system being studied. Hence, the highest possible entropy would occur when each microstate is possible and has an equal probability. Suppose we have a system with n possible configurational states; for the maximum possible entropy, each configuration will have an equal probability, $p_i = 1/n$. We can derive the upper limit for the configurational entropy by directly substituting into the Gibbs Entropy formula (Equation 20):

$$S_{Max} = -\mathrm{k_B} \sum_{i=i}^{n} \frac{1}{n} \ln\left(\frac{1}{n}\right) = -\mathrm{k_B} n * \tfrac{1}{n} ln\ \left(\tfrac{1}{n}\right) = \mathrm{k_B} ln\,(n) \tag{21}$$

However, in practice the probabilities p_i are not equal, as not all configurations correspond to unique energies (for example, in the case of finding two symmetric arrangements). Furthermore, in real systems, lower energy configurations are more likely than higher energy ones. In order to calculate a more realistic p_i we must determine the DOS for the system, by calculating the energies for all configurations. We denote the counts at a given energy as g_i, (the DOS in a discrete form). Subsequently we multiply by the Boltzmann distribution to account for lower energies being more likely. We come to the following equation:

$$p_i = \frac{g_i\, e^{-\frac{E_i - E_0}{\mathrm{k_B} T}}}{Z}, Z = \sum_{i=1}^{n} g_i\, e^{-\frac{E_i - E_0}{\mathrm{k_B} T}} \tag{22}$$

$$S_{conf} = -\mathrm{k_B} \sum_{i=1}^{n} \frac{g_i\, e^{-\frac{E_i - E_0}{\mathrm{k_B} T}}}{Z} \ln\left(\frac{g_i\, e^{-\frac{E_i - E_0}{\mathrm{k_B} T}}}{Z}\right) \tag{23}$$

where T is the temperature of the material (at synthesis), E_0 the ground state energy out of all configurations, and E_i is the total energy that corresponds to the counts g_i.

It should be noted that calculating the configurational entropy of materials using computational methods has been a challenging problem in materials science, as determining entropy would require determining the configurational density of states (DOS), which is computationally infeasible using methods such as DFT as it would require numerous calculations [53]. Therefore, we calculate the Coulomb energies of different configurations as a computationally more feasible substitute for calculating their DFT energy. Entropy calculated using Coulomb energies assumes that there is a direct proportion between change in Coulomb energy and the change in total energy of the system. This method is justifiable in an ionic system such as a layered oxide, where the Electrostatic interaction dominates. Hence in our model, the energies E_i are represented by Coulomb energies.

We can apply this methodology to $NaMn_{0.25}Fe_{0.25}Co_{0.25}Ni_{0.25}O_2$. Coulomb energies E_i were obtained by randomly generating configurations (close to the maximum possible number of configurations for the system) using the Electrostatics optimization software GOAC [50]. Possible inaccuracies may arise from some

16146840, 2026, 42, Downloaded from https://advanced.onlinelibrary.wiley.com/doi/10.1002/aenm.202505470 by Forschungszentrum Juelich Gmbh, Wiley Online Library on [17/11/2026]. See the Terms and Conditions (https://onlinelibrary.wiley.com/terms-and-conditions) on Wiley Online Library for rules of use; OA articles are governed by the applicable Creative Commons License

configurations being sampled multiple times in the dataset. When modelling the structures, $2 \times 2 \times 1$ supercells were used such that the O3 structure had a total of 48 atoms in the supercell, 12 of which are TM atoms (N = 12) and the P2 supercell contained a total of 32 atoms, 8 of which were TM atoms. For the P2 structure, 3×10^7 random configurations were generated, while for the O3 structure 3×10^5 random configurations were generated, due to the different number of possible configurational states for the structures. To analyze the effect of entropy on the stability of each phase, the Gibbs free energy ($G = U\text{-}TS\text{+}pV$) between O3 and P2 structure was computed. The internal energy U was estimated by calculating the total energy of the lowest Coulomb energy configuration of O3 and P2 systems using density functional theory (DFT) relaxation. The calculation was done using the Vienna ab initio Simulation Package (VASP) [54, 55] using the projector augmented wave (PAW) method [56], with energy cutoff 520 eV, the Perdew-Burke-Enzerhof (PBE) exchange-correlation functional [57], force difference of 0.02 eV/Å for ionic convergence, and energy difference of 10^{-5} eV for electronic convergence. The pV term can be neglected for solid phases. The results of these computations are discussed in section 3.5. As the example system studied contains TMs, and the bare PBE functional has been known to exhibit over-delocalization errors [58], for comparison and verification DFT+U (developed by Anisimov, Zaanen and Andersen in Ref. [59]) minimum energies were also calculated using several Hubbard U values. Furthermore, since the Gibbs free energy is plotted for high temperatures, vibrational entropy contributions should also be considered. Vibrational entropy contributions to the Gibbs free energy were calculated with the finite displacement method using Phonopy package [60] and VASP (PBE exchange correlation functional).

3 | Results and Discussion

3.1 | Preferred Phase of Layered Cathode Materials in SIBs

First, we examined the validity of the linear classification model, the cationic potential approach, reported by Zhao et al. [7]. Figure S1a shows the distribution of the 104 samples of the original work in the ϕ_{Na}-ϕ_{cation} space. Three P2-type materials were misclassified as O3-phase. Meanwhile, seven O3-type materials were misclassified as P2-phase, resulting in a model accuracy of 90.38% (see Table S2). To extend the existing database, we collected 166 other layered oxides from the inorganic crystal structure database (ICSD) [61], whose ϕ_{Na}-ϕ_{cation} distribution is shown in Figure S1b. Notably, many of these new compositions have lower Na contents, which were absent from the original database; thus, re-evaluating the model's validity is crucial. The full database used in this work is listed in Table S1. Our results indicate that four P2-type compounds and fifteen O3-type compounds were misclassified (Table S2). Consequently, the linear classification model exhibits a P2 bias, wherein additional O3-type compositions, especially those with lower Na content, are incorrectly classified as P2-type, and the overall accuracy drops to 88.55% on the newly collected dataset, which includes 166 compositions.

Overall, the linear classification model shows 89.26% accuracy on the complete dataset of 270 layered oxide materials (Figure S1c), with misclassifications involving seven P2-type and twenty-two O3-type samples (Figure S1d, compositions shown in Table S2). We refitted, the linear model parameters from Ref. [7] yielding values of 0.406 and 1.579 which are almost identical to the original values (0.407 and 1.572) proving the predictive power of the cationic potential model reported in Ref. [7]. Although the model proposed in Ref. [7] achieves strong performance within a simple 2D model, it can be limited by its reliance on only two descriptors (ϕ_{Na} and ϕ_{cation}). Moving beyond a linear classification using only two features may address these issues by adopting more complex techniques and incorporating additional descriptors.

3.2 | Binary Classification of Preferred Phase Based on Machine Learning

Figure 1 depicts the schematic workflow of this study, which aims to extract higher-dimensional features from the compositions of layered oxide materials. Various machine learning techniques are then employed as binary classifiers to predict whether each layered oxide prefers the O3 or P2 phase. Finally, we evaluate the models by calculating relevant metrics, aiming to propose improved approaches for phase prediction and to glean chemical and physical insights that can inform material design. For feature engineering, we proposed five fundamental properties, concentration (n), ionic radius (r), charge (q), ionic potential (ϕ), and ionization energy (I) for each element. Because different layered oxides may contain different element types, constructing a uniform feature set is challenging. For example, $NaNi_{1/4}Co_{1/4}Fe_{1/4}Mn_{1/8}Ti_{1/8}O_2$ has five different transition metals (Ni, Co, Fe, Mn, Ti), whereas $NaCoO_2$ has only Co in the TMO_2 layer. Explicitly representing each transition metal and its possible oxidation states would greatly expand the dimensionality of the feature set and risk overfitting while complicating model interpretability. To address this, we reduced the dimensionality of the TM features to five: n_{TM}, r_{TM}, q_{TM}, ϕ_{TM}, and I_{TM}. Each represents a weighted average of the property values of all TMs present, with weights proportional to their concentrations (Equations 2–6). We also introduced the mixing entropy of the TMs (S_{TM}), defined by the classical formulation for mixing ideal species (Eq. 8), to indicate how many types of elements occupy the TMO_2 layer and their proportions. Additionally, we continued to include the cationic potential (ϕ_{cation}) as defined in Ref. [7]. Although seventeen features were initially proposed, many of them are linearly correlated and can be reduced. For instance, the charge, ionic potential, and ionization energy of Na ions weighted by their concentration are directly proportional to the concentration of Na, while oxygen-related features are unnecessary because the oxygen content is fixed at two in the whole dataset. The correlation between two arbitrary features can be evaluated by calculating the Pearson correlation coefficients, as illustrated in Figure S2. We excluded features that have no variance (i.e., constant) and those that are linearly correlated with other features, as they do not influence the model. As a result, six linearly independent features (with Pearson correlation coefficients not equal to ±1) were identified: the concentration of Na (n_{Na}), weighted TM radius (r_{TM}), average TM ionic potential (ϕ_{TM}), ionization energy (I_{TM}), and the mixing entropy of TMs (S_{TM}), and the cationic potential (ϕ_{cation}), as shown in Figure S3.

16146840, 2026, 42, Downloaded from https://advanced.onlinelibrary.wiley.com/doi/10.1002/aenm.202505470 by Forschungszentrum Juelich GmbH, Wiley Online Library on [17/11/2026]. See the Terms and Conditions (https://onlinelibrary.wiley.com/terms-and-conditions) on Wiley Online Library for rules of use; OA articles are governed by the applicable Creative Commons License

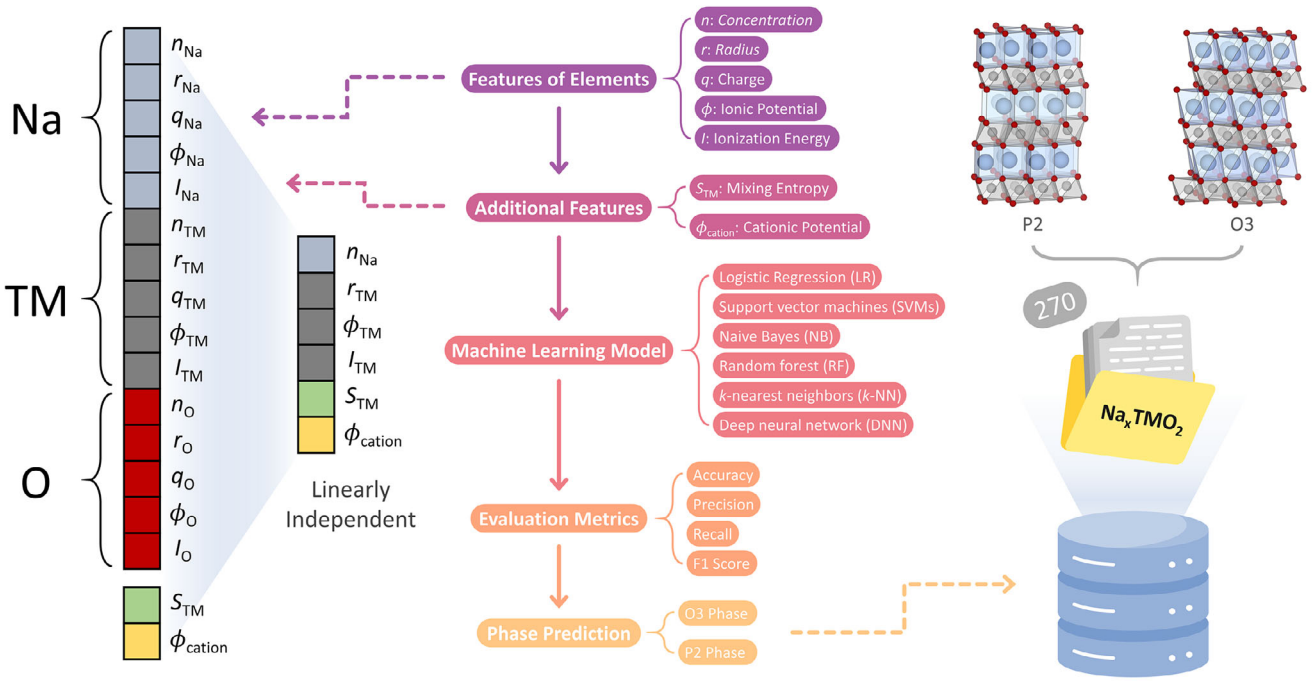


FIGURE 1 | Schematic illustration of the workflow in this study, encompassing feature selection, inputting these features into ML models, and predicting the preferred phase of layered oxides.

We applied six common machine learning techniques, LR, SVM, NB, RF, *k*-NN, and DNN, to perform binary classification of the preferred phase (O3 or P2) in layered oxides and employed K-fold cross-validation for LR, SVM, NB, and *k*-NN to mitigate overfitting. Furthermore, we aimed to develop a model that predicts the preferred phase of layered oxides based solely on their chemical formula. Therefore, traditional classification models (LR, SVM, NB, RF, *k*-NN, and DNN) are most suitable for this task. The full dataset contains 151 P2-type and 119 O3-type compositions, with a P2-to-O3 ratio of approximately 1.27:1. This indicates that the number of P2-type and O3-type samples is comparable, and thus the dataset is not expected to suffer from severe class imbalance. We evaluated the models using four metrics derived from confusion matrices: accuracy, recall, precision, and F1 score, as shown in Equations 9–12. Although accuracy is the overall rate of correct predictions, it can be misleading in the presence of class imbalance. Recall is the proportion of true O3 compositions correctly classified, while precision is the proportion of predicted O3 compositions that are actually O3. A model exhibiting a P2 bias tends to increase false P2 classifications and decrease false O3 classifications, leading to lower recall and higher precision. Conversely, an O3 bias has the opposite effect. For example, the linear classification model proposed in Ref. [7] achieves a recall of 0.8150 and a precision of 0.933, providing clear evidence of a P2 bias. The F1 score, defined as the harmonic mean of precision and recall, only becomes high when both metrics are high. The F1 score for the linear model in Ref. [7] is 0.8700.

We first used the LR model as the classifier and varied the inverse of the regularization strength (hyperparameter) from 0.001 to 10, selecting the F1 score for optimization. As shown in Figure S4, the F1 score peaked at 0.8541 when the inverse of the regularization strength was 0.05, yielding an accuracy, precision, and recall of 0.8852, 0.9475, and 0.7909, respectively. Although precision increased, recall decreased further. Next, we examined the SVM model by tuning the penalty parameter for the error term (Figure S5), finding an optimal value of 100, where the F1 score reached 0.8677. In comparison to LR, SVM offered higher accuracy (0.8963), precision (0.9631), and recall (0.7992), demonstrating better phase prediction. The NB model showed an accuracy of 0.8778, a precision of 0.9271, a recall of 0.7902, and an F1 score of 0.8471, indicating its unsuitability for this task. The NB approach relies on the assumption of conditional independence among features, which is clearly violated here since the cationic potential correlates strongly with the ionic potential of Na and TMs, and the ionic potential itself depends on the charge and radius. Regarding the RF model, we varied the number of estimators and found that the F1 score improved to 0.8800 and remained steady when the number of estimators exceeded 5 (Figure S6). We, therefore, chose 5 estimators to limit computational costs. Notably, the RF model boosted the recall to 0.9167 but lowered the precision to 0.8462, indicating an O3 bias with falser O3 classifications than false P2 ones, the opposite tendency to most other models. Finally, for the *k*-NN model, we plotted the F1 score as a function of the number of neighbors *k* (Figure S7). The F1 score rose as *k* increased from 1 to 5, then declined as *k* increased from 5 to 11, the optimal *k* was set to 5. This yielded performance similar to LR, with accuracy, precision, recall, and F1 scores of 0.8889, 0.9413, 0.7992, and 0.8608, respectively.

Given that the five machine learning models, LR, SVM, NB, RF, and *k*-NN, did not perform optimally and failed to significantly improve all the evaluation metrics, we turned to a more complex model. We employed a DNN classifier, as illustrated in Figure S8a, which shows the database splitting strategy and the DNN architecture. Three distinct datasets were established: the training set was used for model training via backpropagation

16146840, 2026, 42, Downloaded from https://advanced.onlinelibrary.wiley.com/doi/10.1002/aenm.202505470 by Forschungszentrum Juelich GmbH, Wiley Online Library on [17/11/2026]. See the Terms and Conditions (https://onlinelibrary.wiley.com/terms-and-conditions) on Wiley Online Library for rules of use; OA articles are governed by the applicable Creative Commons License

and weight updates; the validation set was used to determine hyperparameters (number of epochs) by calculating the model loss at each epoch without participating in backpropagation; and the testing set, containing entirely unseen data, was used to evaluate the model's performance and generalization ability at the end of training. Specifically, 10% of the data (27 samples) was assigned to the testing set; from the remaining data, 5% (13 samples) was used as a validation set to determine the training epochs and prevent overfitting; the remaining 230 samples were used for training. The DNN model consists of an input layer with six standardized features, followed by four hidden layers containing 12, 8, 6, and 3 neurons, respectively, and concludes with an output layer featuring a single neuron that uses a sigmoid activation function to yield the probability of a composition being an O3-type layered oxide. This architecture allows the model to capture complex feature interactions. The design expands the dimension of the hidden layers first, enabling the extraction of higher-dimensional features, and then gradually reduces it to interface with the single-neuron output layer. Figure S8b shows the loss evolution for both the training and validation sets over training epochs: the loss dropped sharply from around 1 to 0.25 (training) and 0.35 (validation) in the first 100 epochs and then gradually and steadily decreased thereafter. Around epochs 800–900, both losses stabilized with minor fluctuations. Therefore, we stopped training at 900 epochs. At this point, the losses were approximately 0.14 (training) and 0.21 (validation). Figure S8c,d visualizes the distributions of raw logits (i.e., pre-sigmoid outputs) against the actual phase label (O3-type as 1, P2-type as 0) for the training and validation sets, respectively. The training set achieved an accuracy of 0.9522 (misclassifying 11 out of 230 samples), whereas the validation set showed an accuracy of 0.9231 (misclassifying 1 out of 13 samples). To further evaluate the DNN, we used the unexposed testing set, visualized in Figure S8e. Only one O3-type composition was misclassified as P2-type, yielding an accuracy of 0.9630, a precision of 1.0000, a recall of 0.9167, and an F1 score of 0.9565, indicating excellent classification performance. Even for the full dataset (270 samples), the accuracy, precision, recall, and F1 score reached 0.9519, 0.9907, 0.8992, and 0.9427, respectively. In this scenario, 12 O3-type compositions ($Na_{0.6}Mn_{2/3}Ni_{2/9}Fe_{1/9}O_2$, $Na_{0.622}Fe_{2/3}Mn_{1/3}O_2$, $Na_{0.32}CoO_2$, $Na_{0.695}Mn_{0.5}Ni_{0.39}Fe_{0.1}Mg_{0.01}O_2$, $Na_{0.6}Mn_{0.62}Ni_{0.22}Fe_{0.16}O_2$, $Na_{2/3}Mg_{1/3}Ti_{2/3}O_2$, $Na_{0.8}Fe_{2/3}Mn_{1/3}O_2$, $Na_{0.34}Fe_{2/3}Mn_{1/3}O_2$, $Na_{0.8}Ni_{0.6}Sb_{0.4}O_2$, $Na_{0.52}Fe_{2/3}Mn_{1/3}O_2$, $Na_{0.64}Mn_{0.5}Ni_{0.34}Fe_{0.1}Mg_{0.06}O_2$, $Na_{0.457}Fe_{2/3}Mn_{1/3}O_2$) were misclassified as P2-type, while one P2-type composition ($NaCoO_2$) was misclassified as O3-type, revealing a minor P2 bias.

We summarized four evaluation metrics–accuracy, recall, precision, and F1 score–for all the ML models (Figure 2) and compared them with the linear classification model proposed in Ref. [7]. The LR model slightly improved precision but performed worse on the other metrics. The SVM model increased accuracy and precision but lowered recall and F1 score. The NB model performed the worst in predicting the preferred phase, showing the lowest accuracy, recall, and F1 scores of all models, although its precision exceeded that of the RF model. In contrast, the RF model significantly increased recall to approximately 0.91 but reduced precision to around 0.85, indicating a strong O3 bias. The *k*-NN model behaved similarly to the LR model, achieving only a slight improvement in precision. Notably, the DNN model substantially enhanced all metrics, achieving the highest values among all the models. Therefore, the DNN model is considered the most suitable for this task and was used to perform phase prediction of layered oxide materials. However, a P2 bias remained evident in all models except RF, which exhibited an O3 bias. Although the DNN model still has a mild P2 bias, it significantly reduces misclassifications compared to previous models.

3.3 | Importance and Effects of Features in Classification

Understanding how the selected features affect the classification of the preferred phase is crucial for designing layered oxide materials in SIBs. Figure 3 shows the permutation importance of the six features—ionic potential of TM, Na concentration, mixing entropy of TM, cationic potential, ionization energy of TM, and TM radius—across the six ML models. The LR model primarily identifies the Na concentration and the ionic potential of TM as crucial features, whereas the SVM approach assigns particularly high importance to the Na concentration, followed by the cationic potential. This behavior aligns with the 2D linear classification concept (as shown in Figure S1 and Ref. [7]), which can be considered as a special case of a general SVM. The NB model assigns roughly similar importance to all features. In contrast, the concentration of Na exhibits negligible importance for the RF model, suggesting that it may not effectively capture the influence of Na content. For *k*-NN, the Na concentration, cationic potential, and ionic potential of TM are primarily responsible for classifying unknown samples. Negative permutation importance for the ionization energy of TM in the LR and SVM models signifies that random shuffling of this feature improves the F1 score, suggesting that ionization energy may act as noise or even detract from the models' performance.

Given that the DNN model outperformed all others in this classification task, the corresponding permutation feature importance is expected to most accurately reflect the underlying physicochemical principles governing stacking phase preference. The DNN model ranks the ionic potential of TM highest, followed by the Na concentration, mixing entropy of TM, cationic potential, ionization energy of TM, and TM radius. Benefiting from its multi-layer architecture, the DNN can process high-dimensional input, combining features into abstract representations and thereby using all features. Consequently, cationic potential holds relatively low importance, likely because it can be derived from the ionic potentials of TM and Na, and the ionic potential of Na is proportional to the Na concentration. Thus, the DNN can separate Na and TM's contributions to the phase stability, which may aid future materials design. Notably, the mixing entropy of TM emerges as an influential factor for determining the preferred phase, implying that dopant engineering could play a key role in further studies.

Beyond feature importance, understanding how each feature correlates with the preferred phase is essential for proposing design principles for layered oxides. However, such correlations cannot be derived solely from permutation importance, as it only reveals how the model's performance changes when random noise is introduced to a feature, that is, how important the feature is for prediction. We employed the SHAP method to

16146840, 2026, 42, Downloaded from https://advanced.onlinelibrary.wiley.com/doi/10.1002/aenm.202505470 by Forschungszentrum Juelich GmbH, Wiley Online Library on [17/11/2026]. See the Terms and Conditions (https://onlinelibrary.wiley.com/terms-and-conditions) on Wiley Online Library for rules of use; OA articles are governed by the applicable Creative Commons License

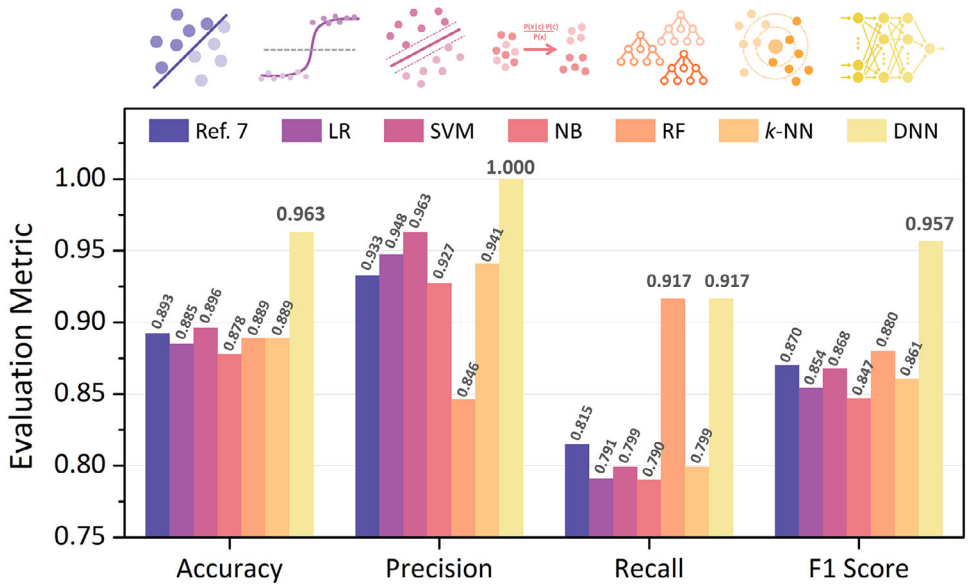


FIGURE 2 | Accuracy, precision, recall, and F1 scores for both the linear classification model reported in Ref. [7] and each ML-based binary classifier—LR, SVM, NB, RF, *k*-NN, and DNN.

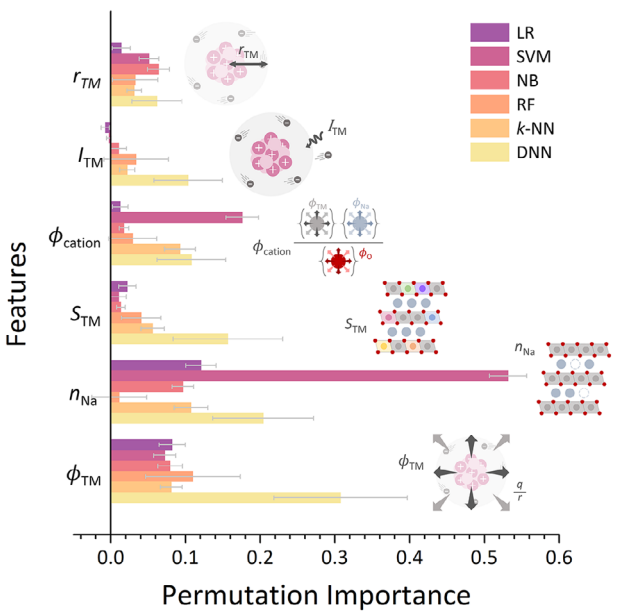


FIGURE 3 | Permutation importance of the six features: ionic potential of TM (ϕ_{TM}), Na concentration (n_{Na}), TM mixing entropy (S_{TM}), cationic potential (ϕ_{cation}), TM ionization energy (I_{TM}), and TM radius (r_{TM}), in each ML-based binary classifier (LR, SVM, NB, RF, *k*-NN, and DNN). The features are plotted in ascending order of their importance in the DNN model.

analyze the correlations between features and the predicted preferred phase, and Figure 4a displays the SHAP summary plot for phase prediction. Positive (negative) SHAP values indicate that the feature drives the classification toward the O3 (P2) phase, while bright yellow and violet colors represent high and low feature values, respectively. Specifically, the SHAP value for each feature causes a shift in the model's output from the baseline (−0.3477) in raw logit space, and the model's output is determined by summing the SHAP values over all features, as shown in Equation 18. Subsequently, the shifted logit passes through the sigmoid function and is nonlinearly projected into the probability of being classified as the O3 class. In the case of the ionic potential of TM, lower feature values (violet and pink dots) generally align with higher positive SHAP values, whereas higher feature values (bright yellow and orange dots) cluster around negative SHAP values; the magnitude of these SHAP values strongly correlates with the feature value. Thus, a high (low) ionic potential of TM favors the P2 (O3) phase in the DNN model. Similarly, compositions with higher concentrations of Na tend to be classified as O3, and those with higher mixing entropy of TM also favor O3 (Figure 4b). The high and low feature values are relative to the mean values of the training set, that is, 0.755 for n_{Na}, 56.525 e·nm^{-1} for ϕ_{TM}, and 0.622 for S_{TM}, since all the features have been standardized before being input into the model. The remaining features, ionization energy of TM, cationic potential, and TM radius, remain important for the DNN model and contribute to its strong performance. However, the SHAP distributions for these features are less straightforward to interpret. The mainstream explanation for how TM ionic potential and Na concentration affect stacking phases is primarily based on the repulsive interactions between adjacent TMO_2 layers [7]. Specifically, a higher TM ionic potential indicates stronger interlayer electrostatic repulsion, favoring the P2 phase. In contrast, a higher Na concentration implies that more Na ions are inserted between TMO_2 layers, enhancing the shielding of interlayer repulsion and thereby stabilizing the O3 phase. Although this explanation aligns with our feature importance and SHAP analyses, the role of TM mixing entropy remains unclear. Moreover, the descriptions of interlayer repulsion and shielding lack detailed atomistic insight. Therefore, in Sections 3.4 and 3.5, we further investigate the TM ionic potential, Na concentration, and TM mixing entropy from an atomistic perspective using ab initio methods.

Figure 4c,d illustrates the distribution of P2- and O3-type compositions, respectively, in the ϕ_{Na}-ϕ_{cation} space, with the

16146840, 2026, 42, Downloaded from https://advanced.onlinelibrary.wiley.com/doi/10.1002/aenm.202505470 by Forschungszentrum Juelich GmbH, Wiley Online Library on [17/11/2026]. See the Terms and Conditions (https://onlinelibrary.wiley.com/terms-and-conditions) on Wiley Online Library for rules of use; OA articles are governed by the applicable Creative Commons License

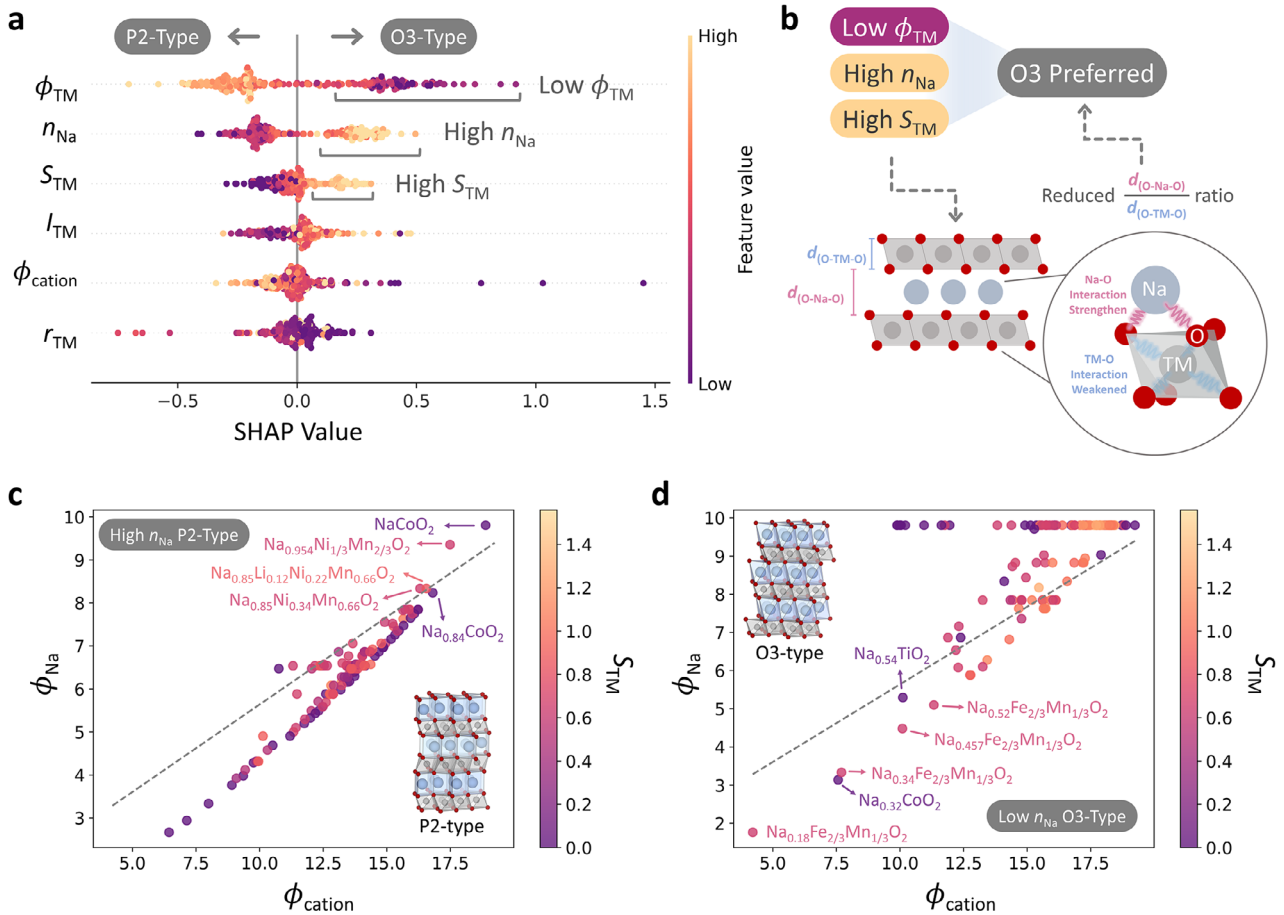


FIGURE 4 | (a) SHAP summary plot for preferred phase prediction in the DNN model, illustrating the SHAP values for each of the six features. (b) Schematic illustration of the three major criteria favoring the O3 phase and the corresponding changes in TM–O/Na–O interaction strength. (c) Distribution of P2-type compositions in the ϕ_{Na}-ϕ_{cation} space, colored by mixing entropy, and (d) distribution of O3-type compositions in the ϕ_{Na}-ϕ_{cation} space, colored by mixing entropy.

data points colored by the mixing entropy of the TM. Several compositions are particularly noteworthy. For example, $NaCoO_2$ appears in the upper right corner of Figure 4c, indicating that its NaO_2 layer is fully occupied by Na, while $Na_{0.18}Fe_{2/3}Mn_{1/3}O_2$ is located in the lower left corner of Figure 4d, where only 18% of the NaO_2 layer is occupied by Na. Based solely on the ionic potential of Na and the cationic potential, $NaCoO_2$ is predicted to be O3-type and $Na_{0.18}Fe_{2/3}Mn_{1/3}O_2$ to be P2-type. However, the TM mixing entropy values for $NaCoO_2$ and $Na_{0.18}Fe_{2/3}Mn_{1/3}O_2$ are 0 and 0.634, respectively. The high mixing entropy observed for $Na_{0.18}Fe_{2/3}Mn_{1/3}O_2$ hints at a different stabilization mechanism, which likely explains why the DNN is able to predict the O3 phase despite the low Na concentration for this material, in agreement with experimental results [62]. It should be noted, however, that the influence of each feature is nonlinear and operates in higher-dimensional space; the simplified low-dimensional projections merely illustrate general trends. Furthermore, exploring layered oxides with high Na content in P2-type structures and low Na content in O3-type structures is crucial, as such compositions are uncommon and bear the potential for interesting novel materials. High-Na-content P2-type oxides are particularly promising for SIBs due to their enhanced structural stability and retention. As shown in Figure 4c, compounds such as $NaCoO_2$, $Na_{0.954}Ni_{1/3}Mn_{2/3}O_2$, $Na_{0.85}Li_{0.12}Ni_{0.22}Mn_{0.66}O_2$, $Na_{0.85}Ni_{0.34}Mn_{0.66}O_2$, and $Na_{0.84}CoO_2$ exhibit high Na contents ($\geq$0.84) despite being stable as P2-type. In contrast, compounds, such as $Na_{0.54}TiO_2$, $Na_{0.52}Fe_{2/3}Mn_{1/3}O_2$, $Na_{0.457}Fe_{2/3}Mn_{1/3}O_2$, $Na_{0.34}Fe_{2/3}Mn_{1/3}O_2$, and $Na_{0.32}CoO_2$, $Na_{0.18}Fe_{2/3}Mn_{1/3}O_2$, exhibit low Na contents ($\leq$0.54) but remain O3-type. Our observations indicate that the O3-type $Na_xFe_{2/3}Mn_{1/3}O_2$ framework can accommodate very low Na levels, whereas P2-type frameworks such as Na_xCoO_2 and $Na_xLi_yNi_{0.34\text{-}y}Mn_{0.66}O_2$ are more suitable for high Na content. The aforementioned high-Na-content P2-type and low-Na-content O3-type compositions have been experimentally synthesized and are included in the ICSD [61]. However, because this data-driven study did not consider detailed electronic properties or explicit interatomic interactions, further investigation of layered oxides based on these frameworks is proposed. Moreover, it must be mentioned that many materials, for example $NaCoO_2$, are reported in both, the O3 structure [63] and the P2 structure [64] experimentally, indicating an additional layer of complexity, which can be the synthesis conditions, that is neither reflected by the cationic potential approach proposed in Ref. [7] nor the DNN model developed in this work. We listed three compositions, that is, $Na_{0.6}Mn_{2/3}Ni_{2/9}Fe_{1/9}O_2$, $Na_{0.6}Mn_{0.62}Ni_{0.22}Fe_{0.16}O_2$, and $NaCoO_2$, which were observed in both P2 and O3 structures, in Table S3. These compositions have not been excluded from our dataset. Consequently, predictions of

16146840, 2026, 42, Downloaded from https://advanced.onlinelibrary.wiley.com/doi/10.1002/aenm.202505470 by Forschungszentrum Juelich GmbH, Wiley Online Library on [17/11/2026]. See the Terms and Conditions (https://onlinelibrary.wiley.com/terms-and-conditions) on Wiley Online Library for rules of use; OA articles are governed by the applicable Creative Commons License

both models should be interpreted with care, even though they allow for reasonable estimations to select novel layered cathode materials. Future machine learning studies might be able to overcome some of these drawbacks by extracting synthesis features from the experimental work and including them in the prediction of the most stable phase. However, much more and especially standardized data would be required for such advanced models.

To test the trained model, we collected 80 additional data points from recent literature beyond the existing online database (Table S4). Among these, 36 P2-type and 44 O3-type compositions were used to examine the reliability of our trained DNN model for state-of-the-art layered oxide materials. These 80 additional data points were absent from the original dataset and are therefore suitable to validate the DNN model. The data distribution per feature of the original 270 compositions used to train the DNN model, along with the newly added data from recent literature, is shown in Figure S9a. Their distributions match closely in all six feature spaces, indicating that our original training dataset can represent the material properties of layered oxides commonly used in recent studies. To examine whether the independent testing data set is collected without bias with respect to the training data set, we conducted principal component analysis (PCA) on both the training data set (270 compositions) and the independent testing data set (80 compositions) used to train and validate the DNN model, respectively. As shown in Figure S9b, the independent testing data set shows significant overlap with the high-density regions of the training set, indicating that the distribution of the independent testing data set is unbiased relative to the training data. Additionally, the PCA confirms that the training set distribution in the feature space covers the range of the independent testing set. Moreover, our model demonstrates high reliability in predicting the stable phase of Na_xTMO_2 materials, with an accuracy of 0.96, precision of 1.00, recall of 0.93, and an F1 score of 0.96. These results are consistent with the testing set from the original dataset of 270 compositions, implying that the trained DNN model has the predictive ability to handle state-of-the-art compositions reported recently, and thus demonstrates high applicability in real-world scenarios. We further estimate the uncertainty of the trained DNN model using the Monte Carlo dropout (MCD) technique, where the dropout layers are activated during the forward pass through the trained network [65]. This forward pass is repeated 1000 times. Since the output of the DNN model varies slightly with each forward pass when the dropout layer is active, the uncertainty and probability of being classified as O3 can be calculated based on the 1000 iterations (Table S4). Notably, the prediction results for the independent data set remain consistent with those obtained when the dropout layer was deactivated. However, the uncertainty for $Na_{0.75}Fe_{0.25}Cu_{0.25}Mn_{0.5}O_2$, $Na_{0.65}Mn_{0.4}Ni_{0.3}Fe_{0.15}Li_{0.1}Ti_{0.05}O_2$, and $Na_{0.55}Mn_{0.4}Ni_{0.3}Fe_{0.15}Li_{0.1}Ti_{0.05}O_2$ was 0.18, 0.09, and 0.10, respectively, indicating that the model has relatively higher uncertainty for these three misclassified compositions. The scatter plot of the true stacking phases for all 350 compositions, sourced from Ref. [7], the ICSD database [61], and reported literatures, is shown in Figure S10. The compositions that were correctly predicted and those that were misclassified are denoted by blue circles and red crosses, respectively. The misclassified compositions are labeled with their sample IDs, as listed in Tables S1 and S4.

To further demonstrate our hypothesis regarding the TM mixing entropy, we compared a few specific compositions. The O3-type $Na_{0.8}Ni_{0.2}Fe_{0.2}Co_{0.2}Mn_{0.2}Ti_{0.2}O_2$ shows excellent cycling stability with over 90% capacity retention after 100 cycles, as reported by Nam et al. [66]. We compared it with three other P2-type compositions, including $Na_{0.85}Ni_{0.34}Mn_{0.66}O_2$ [67], $Na_{0.85}Li_{0.12}Ni_{0.22}Mn_{0.66}O_2$ [67], and $Na_{0.8}Mn_{0.6}Co_{0.4}O_2$ [68], since they have similar features in TM ionic potential, Na concentrations, TM ionization energy, cationic potential, and TM radius, as shown in Figure S11. Based on the aforementioned SHAP analysis, these compositions should have the same preferred phase. However, both experimental results and predictions confirmed that $Na_{0.85}Ni_{0.34}Mn_{0.66}O_2$, $Na_{0.85}Li_{0.12}Ni_{0.22}Mn_{0.66}O_2$, and $Na_{0.8}Mn_{0.6}Co_{0.4}O_2$ are P2-type, while $Na_{0.8}Ni_{0.2}Fe_{0.2}Co_{0.2}Mn_{0.2}Ti_{0.2}O_2$ is O3-type. This can be explained by their significantly different TM mixing entropy values. Specifically, O3-$Na_{0.8}Ni_{0.2}Fe_{0.2}Co_{0.2}Mn_{0.2}Ti_{0.2}O_2$ has a TM mixing entropy of 1.609, while the other three compositions have values ranging from 0.64 to 0.86, thus favoring the P2 phase. Hence, the importance of the TM mixing entropy feature, is not only concluded from our SHAP analysis, but is also backed-up by experimental observations.

Finally, it should be noted that the DNN proposed in this work allows for a reasonable prediction of which stacking phase (O3 or P2) can be obtained in an experiment with an overall higher accuracy than previous approaches, thus enabling high-throughput predictions to identify promising novel layered oxide Na-ion battery cathode materials (e.g., low Na content O3-type $Na_xFe_{2/3}Mn_{1/3}O_2$, high Na content P2-type Na_xCoO_2, and $Na_xLi_yNi_{0.34-y}Mn_{0.66}O_2$). However, our model was trained on experimentally synthesized P2- and O3-type compositions, and potential phase transitions during charging and discharging were not considered. Such transitions are more complex and depend on additional factors (e.g., charge/discharge rate, cut-off voltage, and state of desodiation) and should be examined in future work by constructing a new network with modified dimensions to better evaluate battery performance. Meanwhile, other stacking variants (e.g., P3, O2, P′2, O′3) [6, 69] and the P2/O3 mixed-phase [70–72] were excluded because far fewer compositions have been reported than for P2 and O3, which would introduce severe class imbalance and yield unreliable predictions [73]. Incorporating these phases will be more feasible once comparable numbers of compositions become available. Another limitation is that the features focus solely on the composition to simplify the input requirements for prediction, while features related to the synthesis process, such as temperature, precursor, and methods, are lacking. For example, residual alkali species on the cathode surface have been shown to significantly affect the interfacial stability of the cathode [74–76]. Therefore, monitoring different chemicals during the synthesis process is also crucial for understanding the effect of the synthesis method on stacking phase preference and for further improving the features and the model's predictive ability.

3.4 | Electrostatics

The feature values for four well distinguishable compounds, namely $NaTiO_2$, $Na_{0.78}Ni_{0.23}Mn_{0.69}O_2$, $Na_{0.667}Mn_{0.833}O_2$, and $Na_{0.7}Ni_{0.35}Sn_{0.65}O_2$ are visualized in Figure 5. We have chosen

16146840, 2026, 42, Downloaded from https://advanced.onlinelibrary.wiley.com/doi/10.1002/aenm.202505470 by Forschungszentrum Juelich Gmbh, Wiley Online Library on [17/11/2026]. See the Terms and Conditions (https://onlinelibrary.wiley.com/terms-and-conditions) on Wiley Online Library for rules of use; OA articles are governed by the applicable Creative Commons License

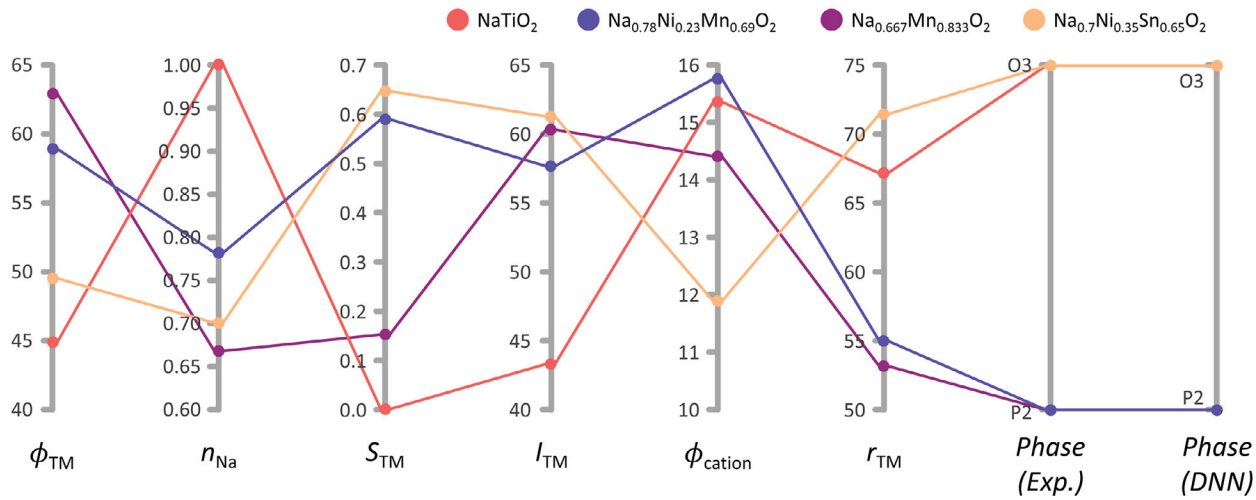


FIGURE 5 | (a) Values of the six features and resulting experimentally measured and predicted phases of four selected compositions: $NaTiO_2$, $Na_{0.78}Ni_{0.23}Mn_{0.69}O_2$, $Na_{0.667}Mn_{0.833}O_2$, and $Na_{0.7}Ni_{0.35}Sn_{0.65}O_2$.

compositions with distinct ϕ_{TM} values for which experimentally obtained phase is in accordance with the DNN prediction. Results indicate that the higher the ionic potential, the more likely it is that P2 phase is formed.

As demonstrated above, the DNN model revealed that ϕ_{TM} has the highest importance in predicting the favored phase. The second most relevant feature is n_{Na}. To further investigate the results of the DNN model, in particular how the relevant features are interrelated, we perform electrostatic calculation and analysis on compounds characterized by distinct values of ionic potential ϕ_{TM}: $NaTiO_2$ with ϕ_{TM} = 44.78 e·nm^{-1}, $Na(Vac_{0.08})Ni_{0.25}Mn_{0.67}O_2$ possessing ϕ_{TM} = 53.7474 e·nm^{-1}, and $Na_{0.67}(Vac_{0.08})Ni_{0.25}Mn_{0.67}O_2$ characterized by ϕ_{TM} = 61.66 e·nm^{-1}. The electrostatic calculation is used to i) confirm the values of charges for ions with multiple oxidation states employed when calculating features that serve as an input for the ML workflow and ii) gain insights into the ionic potential, recognized to be the dominant feature for prediction of phase stability. Analysis of the pairwise ion-ion electrostatic interaction can unveil the physical reasons that determine the phase stability in a range of chemical compounds.

The computed relative difference in electrostatic energy between the P2 and O3 phases is shown in Figure 6. Our analysis for $NaTiO_2$ and $Na(Vac_{0.08})Ni_{0.25}Mn_{0.67}O_2$ reveals that their O3 stacking is more stable than their P2 stacking by 43 and 31 meV, respectively. This result aligns with the prediction of the DNN model in which O3 was predicted to be more stable than P2 for compositions with higher values of n_{Na}. It also provides quantitative evidence that increased Na concentration enhances the shielding of repulsive interactions between TMO_2 layers, thereby favoring the O3 phase over the P2 phase.

In the next step, we consider the compound described by the highest value of ϕ_{TM}, that is, $Na_{0.67}(Vac_{0.08})Ni_{0.25}Mn_{0.67}O_2$. Electrostatic calculations indicate that the P2 phase is significantly more stable than the O3 phase (by more than 60 meV). The XRD analysis clearly confirms the dominance of the P2-type structure on similar Mn-deficient layered oxides ($Na_{0.78}(Vac_{0.08})Ni_{0.23}Mn_{0.69}O_2$

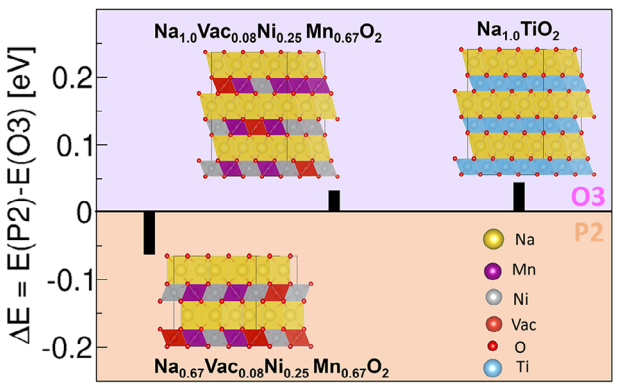


FIGURE 6 | Computed total electrostatic energy difference ΔE (in eV) between P2 and O3 phases for three representatives of layered oxide compounds, $Na_{0.67}Vac_{0.08}Ni_{0.25}Mn_{0.67}O_2$, $Na_{1.00}Vac_{0.08}Ni_{0.25}Mn_{0.67}O_2$, and $NaTiO_2$ characterized by their distinct values of ionic potential ϕ_{TM}. The stability regions of P2 and O3 phases are highlighted in orange and purple, respectively. Minimum-energy atomic structures for each composition are provided as well.

[77]). The P2 phase has been predicted to be more stable based on a recent first-principles calculation on a similar composition, namely $Na_xNi_{0.25}Mn_{0.68}O_2$ [78], which is in agreement with our electrostatic calculations and DNN derived model. Our electrostatic analysis on $NaTiO_2$, $Na(Vac_{0.08})Ni_{0.25}$ $Mn_{0.67}O_2$, and $Na_{0.67}(Vac_{0.08})Ni_{0.25}Mn_{0.67}O_2$ confirms the trend deduced from the DNN model that a low ionic potential of TM favors the O3 phase, while a high value of ionic potential works in favor of the P2 phase.

Furthermore, we investigated the pairwise ion-ion interactions by calculating the electrostatic energy difference between the P2 and O3 phases of the corresponding pair (see Figure 7). Interactions between Na and TM as well as Na-Na are found to be strongly Na concentration dependent. At the Na concentration of 2/3, a high Mn^{4+} concentration of 100% (i.e., high ionic potential) stabilizes P2 over O3 through Na-TM interaction in $Na_{0.67}(Vac_{0.08})Ni_{0.25}Mn_{0.67}O_2$. Figure 7 shows that for

16146840, 2026, 42, Downloaded from https://advanced.onlinelibrary.wiley.com/doi/10.1002/aenm.202505470 by Forschungszentrum Juelich GmbH, Wiley Online Library on [17/11/2026]. See the Terms and Conditions (https://onlinelibrary.wiley.com/terms-and-conditions) on Wiley Online Library for rules of use; OA articles are governed by the applicable Creative Commons License

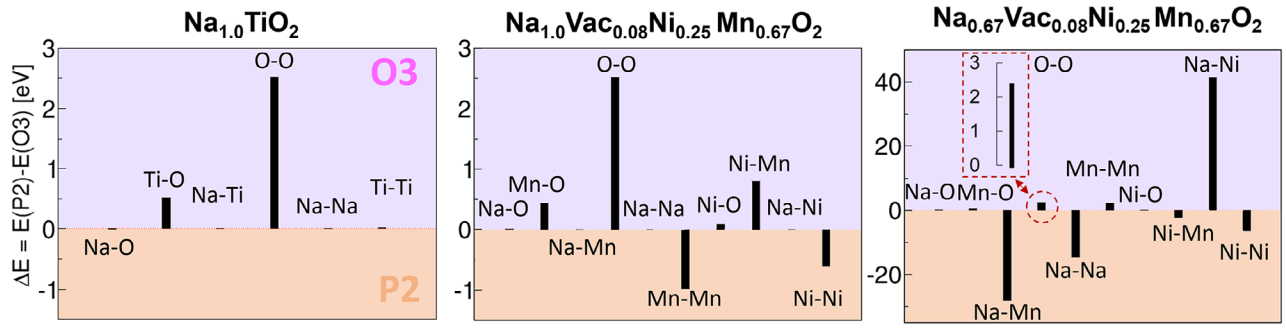


FIGURE 7 | Computed pairwise electrostatic energy difference ΔE (in eV) between the P2 and O3 phases for three selected compounds (see Figure 6). The stability regions of P2 and O3 phases are highlighted in orange region and purple, respectively.

this composition Na-Mn^{4+} favors P2, while Na-Ni^{2+} does O3. At high Na-concentration of 1.0 this preference vanishes. The other important interaction is Na-Na whose energy at low Na concentration is lower for the P2 phase. However, at high Na concentration of 1.0 no significant phase preference through Na-Na interactions is found, because the same arrangement of Na ions can be achieved in both phases. On the other hand, O-O interactions always prefer the O3 phase for which O-O interlayer distances are longer (weaker O-O repulsion). Therefore, the higher stability of P2 phase for $Na_{0.67}(Vac_{0.08})Ni_{0.25}Mn_{0.67}O_2$ is dictated by more favorable Na-Mn^{4+} and Na-Na interactions in this phase compared to O3 in spite of higher stability of O3 over P2 through O-O interactions. As mentioned before, since at a high Na concentration there is no preference of P2 over O3 through Na-TM^{4+} (lowering of ϕ_{TM} with decreasing TM^{4+} concentration to 75% and 0%) and Na-Na interaction (determined by n_{Na}), the O-O interaction stabilizes the O3 phase in both $Na(Vac_{0.08})Ni_{0.25}Mn_{0.67}O_2$ and $NaTiO_2$, respectively.

3.5 | Entropy Estimation

Results of the DNN suggested that high S_{TM} favors the O3 phase. In order to investigate the effect of configurational entropy on phase stability, we modeled the P2 and O3 phase of $NaMn_{0.25}Fe_{0.25}Co_{0.25}Ni_{0.25}O_2$ (a system with high S_{TM}) and calculated the Coulomb energies of possible atomistic configurations to estimate its configurational entropy. $NaMn_{0.25}Fe_{0.25}Co_{0.25}Ni_{0.25}O_2$ was synthesized in the O3 phase [79] and also predicted by the DNN as O3. S_{TM} for the composition is 1.386.

Computed DOS for this composition in both phases (O3 and P2) are shown in Figure 8a. The mixing entropy (for ideal gasses) (Equation 19), maximum configurational entropy (Equation 21), and actual estimated entropy (Equation 22) for the unit cells are summarized in Table 1. Entropy values are given per formula unit (F.U.). The calculated configurational entropy is 0.0349 meV/K and 0.0118 meV/K per F.U. for the O3 and P2 unit cells, respectively. Even though the P2 structure has many Na sites and a much higher n, it shows a lower entropy than the O3 structure. A reason for this could be that the P2 structure had many configurations with an energy much higher than the ground state—at full Na concentration, many configurations exist in which both Na sublattices are occupied. These configurations are very high in energy due to short Na-Na distance, and are thus unfavorable. We therefore observe that although the O3 system does not have any states with $(E_i—E_0)/N > 6$, the P2 system has many more high energy states.

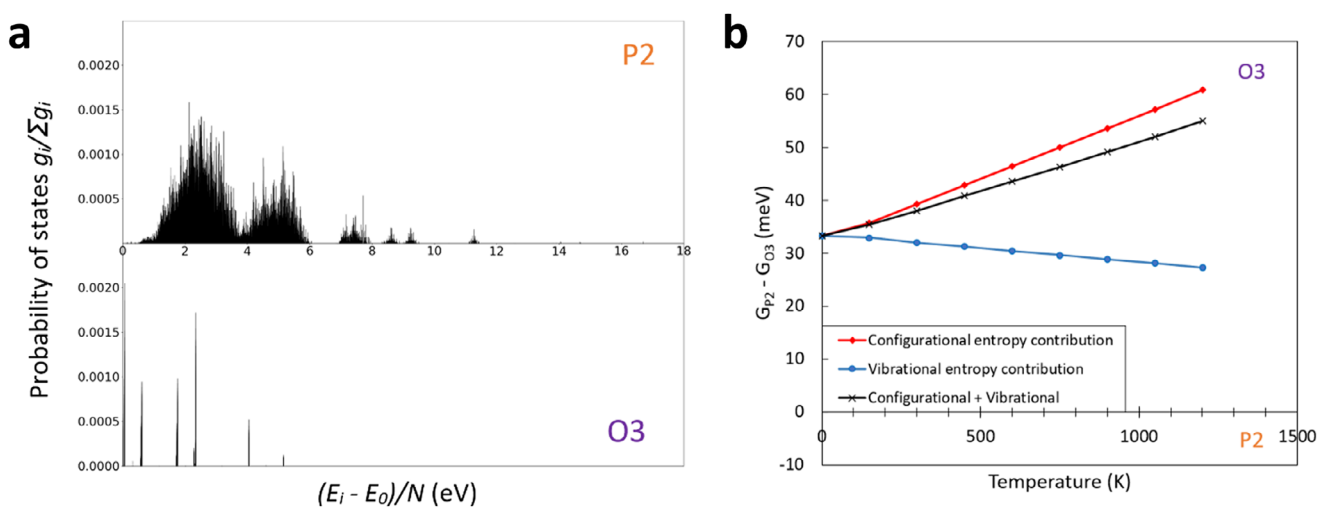


FIGURE 8 | (a) Configurational density of states (DOS) for P2 (top) and O3 (bottom) phases of $NaMn_{0.25}Fe_{0.25}Co_{0.25}Ni_{0.25}O_2$ structure, with normalized g_i. (b) Gibbs free energy difference between P2 (G_{P2}) and O3 (G_{O3}) phases of $NaMn_{0.25}Fe_{0.25}Co_{0.25}Ni_{0.25}O_2$ as a function of temperature for the vibrational entropy component, configurational entropy component, and combined configurational and calculated vibrational entropy contributions.

16146840, 2026, 42, Downloaded from https://advanced.onlinelibrary.wiley.com/doi/10.1002/aenm.202505470 by Forschungszentrum Juelich GmbH, Wiley Online Library on [17/11/2026]. See the Terms and Conditions (https://onlinelibrary.wiley.com/terms-and-conditions) on Wiley Online Library for rules of use; OA articles are governed by the applicable Creative Commons License

TABLE 1 | Calculated configurational entropies for P2-$NaMn_{0.25}Fe_{0.25}Co_{0.25}Ni_{0.25}O_2$ and O3-$NaMn_{0.25}Fe_{0.25}Co_{0.25}Ni_{0.25}O_2$ per formula unit (F.U.) We note that even though the O3 structure had a larger unit cell, it had much fewer possible combinations n, due to the fact that P2 structures have twice as many sodium sites available. The temperature T used is 1200K, comparable to the synthesis temperature for this material [79].

Phase	O3	P2
n **(possible combinations)**	3.696×10^5	3.243×10^7
N **(TMs)**	12	8
$S_{Mix\ (ideal\ gas)}$ **per F.U. (meV/K)**	0.119	0.119
S_{Max} **per F.U. (meV/K)**	0.092	0.186
S_{config} **per F.U. (meV/K)**	0.0349	0.0118

TABLE 2 | DFT+U energy difference between P2 and O3 $NaMn_{0.25}Fe_{0.25}Co_{0.25}Ni_{0.25}O_2$ for several U values. A positive value indicates P2 has a higher energy than O3, thus the O3 phase is more energetically favored. U-values were taken from Ref. [80] for the corresponding TM-oxide with oxidation state 2+ for Ni (U-value 4.40 eV), 3+ for Fe (4.09 eV) and Co (4.26 eV), and 4+ for Mn (3.19 eV). For the remaining results, an identical U value (2, 3, 4, or 5 eV) was assigned to each TM.

U-value	E(P2)—E(O3) [meV]
0	33.26
Ref. [80]	145.52
2	25.65
3	−45.11
4	190.86
5	223.30

Table 2 shows the P2 and O3 energy differences when applying different Hubbard U corrections to the bare PBE functional. The results support that the relative P2-O3 energy differences are largely insensitive to adding a Hubbard U correction. The most justifiable U-values taken from Ref. [80], which are calculated by fitting parameters to experiment, support O3 stability for this composition, while a U-value of 3 eV for all TMs favors P2 stability. However, values of 2, 4, and 5 eV show the same trend as the values taken from literature and the bare PBE functional.

We also note that for the P2 structure, the mixing entropy (ideal gas) is lower than S_{Max}. Although in principle, the ideal gas entropy should be higher than S_{Max}, the formula for S_{Mix} only takes into account the TM occupations, and does not consider the fact that for a P2 material there are twice the Na sites available than for O3 (for the same number of Na atoms). This contributes significantly to the number of possible configurations n and thus to S_{Max}. Overall, the calculated entropy contributions for both compositions are less than 1 meV/K.

Finally, the Gibbs free energy difference as function of temperature is plotted in Figure 8b. For the material, it is found that the O3 phase is Enthalpy-driven, as $\Delta G = G_{P2}$-G_{O3} at 0K is positive. Figure 8b indicates that with increasing temperature, the Gibbs free energy difference increases further due to the higher entropy calculated for the O3 system. Studying the difference in thermal vibrations of the P2 and O3 phase shows the vibrational entropy difference is at a similar order of magnitude for both phases. Therefore, despite the small value of the configurational entropy it still dominates the temperature dependence of the relative phase stability over the vibrational entropy. These findings support the notion from the machine learning models that for this composition, the entropy contribution favors the O3 phase. Specifically, compositions with higher TM mixing entropy exhibit a greater number of possible low-energy conformations within the configurational space, thereby enhancing the tendency to favor the O3 phase over the P2 phase, an effect that has not been proposed before.

4 | Conclusion

In this work, we developed data-driven models based on machine learning (ML) and ab initio atomistic thermodynamics approaches to predict and understand the phase stability of layered oxides. We constructed a comprehensive phase stability database for layered oxide materials comprising 270 experimental compositions collected from the literature. Compared to existing datasets, our database includes low-Na concentration compositions as well. We proposed six linearly independent features – Na concentration, radius of transition metal (TM), ionic potential of TM, ionization energy of TM, mixing entropy of TMs, and cationic potential – and incorporated these features into six machine learning models (logistic regression (LR), support vector machines (SVMs), naive Bayes (NB), random forest (RF), k-nearest neighbors (k-NN), and deep neural networks (DNNs)). Four evaluation metrics – accuracy, precision, recall, and F1 score – were employed to assess model performance. Our results showed that the simpler models (LR, SVM, NB, RF, and k-NN) cannot significantly improve upon the 2D linear classification method reported in the literature, whereas the DNN model achieved extremely high accuracy (0.9630), precision (1.0000), recall (0.9167), and F1 score (0.9565). Permutation importance analysis revealed that the TM ionic potential, Na concentration, and TM mixing entropy are the major factors influencing the DNN model, while SHAP analysis indicated that a lower (higher) TM ionic potential, higher (lower) Na concentration, and higher (lower) TM mixing entropy, relative to the corresponding mean values, favor classification as O3 (P2)-type. Focusing on selected compositions with distinguishable features from DNN predictor, we studied the physical meaning of determined features and their role in controlling the phase stability. DFT and electrostatic calculations confirm the DNN-based results. Analysis of pairwise interactions shows that Na-TM and Na-Na interactions are main factors in determining the phase preference in layered oxide materials. Both of these parameters are Na-concentration dependent validating the importance of this ML-determined feature. Besides Na concentration, the Na-TM interaction depends strongly on the charge state of TM which is one of the ionic potential parameters. The larger the concentration of TM^{4+}, the more stable is the P2 phase. Our estimated configurational entropy shows that, in line with the DNN predictor, more diverse TM types and concentrations stabilize the O3 phase with increasing temperature. Overall, our efficient DNN-based binary classifier

16146840, 2026, 42, Downloaded from https://advanced.onlinelibrary.wiley.com/doi/10.1002/aenm.202505470 by Forschungszentrum Juelich GmbH, Wiley Online Library on [17/11/2026]. See the Terms and Conditions (https://onlinelibrary.wiley.com/terms-and-conditions) on Wiley Online Library for rules of use; OA articles are governed by the applicable Creative Commons License

and combined ab initio and thermodynamic calculations allow to predict the preferred phase and provide physical insights that enhance the understanding of layered oxide materials to guide future material synthesis.

Acknowledgements

This work was financially supported by the National Science and Technology Council, Taiwan (NSTC 113-2113-M-011-003-MY3, 113-2923-E-011-002, 114-2639-E-011-001-ASP), and the Sustainable Electrochemical Energy Development (SEED) Center funded by the Ministry of Education (MOE), Taiwan, as well as the HIPOBAT project funded by the German Federal Ministry of Research, Technology and Space (BMFTR) under grant number 13XP0611A. Computation time was granted through JARA-HPC on the supercomputer JURECA at Forschungszentrum Jülich under Grant No. jiek12. We further acknowledge support from the UMC Fellowship.

Open access funding enabled and organized by Projekt DEAL.

Conflicts of Interest

The authors declare no conflict of interest.

Data Availability Statement

The complete data of this work is available from the corresponding author upon reasonable request. The dataset of Na_xTMO_2 materials is listed in the Supplementary Materials. The trained DNN model is available in the interactive notebook on Google Colab at [https://github.com/LIANGTING-WU/ML_Phase_Predictor. A graphical user interface (GUI) version of the phase stability predictor is available on Hugging Face Spaces at https://huggingface.co/spaces/LIANGTING-WU/Phase_Predictor.

References

1. B. Dunn, H. Kamath, and J.-M. Tarascon, "Electrical Energy Storage for the Grid: A Battery of Choices," *Science* 334, no. 6058 (2011): 928–935.

2. J. Amici, P. Asinari, E. Ayerbe, et al., "A Roadmap for Transforming Research to Invent the Batteries of the Future Designed Within the European Large Scale Research Initiative BATTERY 2030+," *Advanced Energy Materials* 12, no. 17 (2022): 2102785.

3. Z. Zhu, T. Jiang, M. Ali, et al., "Rechargeable Batteries for Grid Scale Energy Storage," *Chemical Reviews* 122, no. 22 (2022): 16610–16751.

4. Y.-T. Zhan, L.-T. Wu, H. Teng, and J.-C. Jiang, "Unveiling Multi-component Hybrid Organic-inorganic SEI Formation in Gel Polymer Electrolytes: A Computational Study," *Electrochimica Acta* 512 (2025): 145513.

5. J.-Y. Hwang, S.-T. Myung, and Y.-K. Sun, "Sodium-ion Batteries: Present and Future," *Chemical Society Reviews* 46, no. 12 (2017): 3529–3614.

6. C. Delmas, C. Fouassier, and P. Hagenmuller, "Structural Classification and Properties of the Layered Oxides," *Physica B+C* 99, no. 1 (1980): 81–85.

7. C. Zhao, Q. Wang, Z. Yao, et al., "Rational Design of Layered Oxide Materials for Sodium-ion Batteries," *Science* 370, no. 6517 (2020): 708–711.

8. N. A. Katcho, J. Carrasco, D. Saurel, et al., "Origins of Bistability and Na Ion Mobility Difference in P2- and O3-Na 2/3 Fe 2/3 Mn 1/3 O 2 Cathode Polymorphs," *Advanced Energy Materials* 7, no. 1 (2017): 1601477.

9. X. Gao, H. Liu, H. Chen, et al., "Cationic-potential Tuned Biphasic Layered Cathodes for Stable Desodiation/Sodiation," *Science Bulletin* 67, no. 15 (2022): 1589–1602.

10. G. H. Cartledge, "Studies on the Periodic System. II. the Ionic Potential and Related Properties 1," *Journal of the American Chemical Society* 50, no. 11 (1928): 2855–2863.

11. S.-H. Wang, H. S. Pillai, S. Wang, L. E. K. Achenie, and H. Xin, "Infusing Theory Into Deep Learning for Interpretable Reactivity Prediction," *Nature Communications* 12, no. 1 (2021): 5288.

12. T. Koker, K. Quigley, E. Taw, K. Tibbetts, and L. Li, "Higher-order Equivariant Neural Networks for Charge Density Prediction in Materials," *Npj Computational Materials* 10, no. 1 (2024): 161.

13. C. W. Park, M. Kornbluth, J. Vandermause, C. Wolverton, B. Kozinsky, and J. P. Mailoa, "Accurate and Scalable Graph Neural Network Force Field and Molecular Dynamics With Direct Force Architecture," *Npj Computational Materials* 7, no. 1 (2021): 7.

14. M. Yu, S. Yang, C. Wu, and N. Marom, "Machine Learning the Hubbard U Parameter in DFT+U Using Bayesian Optimization," *Npj Computational Materials* 6, no. 1 (2020): 180.

15. S. Batzner, A. Musaelian, L. Sun, et al., "E(3)-equivariant Graph Neural Networks for Data-efficient and Accurate Interatomic Potentials," *Nature Communications* 13, no. 1 (2022): 2453.

16. B. Deng, P. Zhong, K. Jun, et al., "CHGNet as a Pretrained Universal Neural Network Potential for Charge-informed Atomistic Modelling," *Nature Machine Intelligence* 5 (2023): 1031–1041.

17. D. Lemm, G. F. von Rudorff, and O. A. von Lilienfeld, "Machine Learning Based Energy-free Structure Predictions of Molecules, Transition States, and Solids," *Nature Communications* 12, no. 1 (2021): 4468.

18. Y. Yang, O. A. Jiménez-Negrón, and J. R. Kitchin, "Machine-learning Accelerated Geometry Optimization in Molecular Simulation," *The Journal of Chemical Physics* 154, no. 23 (2021): 234704.

19. J. Abramson, J. Adler, J. Dunger, et al., "Accurate Structure Prediction of Biomolecular Interactions With AlphaFold 3," *Nature* 630, no. 8016 (2024): 493–500.

20. J. Jumper, R. Evans, A. Pritzel, et al., "Highly Accurate Protein Structure Prediction With AlphaFold," *Nature* 596, no. 7873 (2021): 583–589.

21. K. Tunyasuvunakool, J. Adler, Z. Wu, et al., "Highly Accurate Protein Structure Prediction for the human Proteome," *Nature* 596, no. 7873 (2021): 590–596.

22. A. D. Sendek, Q. Yang, E. D. Cubuk, K.-A. N. Duerloo, Y. Cui, and E. J. Reed, "Holistic Computational Structure Screening of More Than 12 000 Candidates for Solid Lithium-ion Conductor Materials," *Energy & Environmental Science* 10, no. 1 (2017): 306–320.

23. R. P. Joshi, J. Eickholt, L. Li, M. Fornari, V. Barone, and J. E. Peralta, "Machine Learning the Voltage of Electrode Materials in Metal-Ion Batteries," *ACS Applied Materials & Interfaces* 11, no. 20 (2019): 18494–18503.

24. K. A. Severson, P. M. Attia, N. Jin, et al., "Data-driven Prediction of Battery Cycle Life Before Capacity Degradation," *Nature Energy* 4, no. 5 (2019): 383–391.

25. K. Choudhary and B. DeCost, "Atomistic Line Graph Neural Network for Improved Materials Property Predictions," *Npj Computational Materials* 7, no. 1 (2021): 185.

26. L.-T. Wu, Y.-T. Zhan, Z.-L. Li, P.-T. Chen, B. J. Hwang, and J.-C. Jiang, "Rational Electrolyte Design for Li-metal Batteries Operated Under Extreme Conditions: A Combined DFT, COSMO-RS, and Machine Learning Study," *Journal of Materials Chemistry A* 12, no. 26 (2024): 15792–15802.

27. C.-Y. J. Peng, K. L. Lee, and G. M. Ingersoll, "An Introduction to Logistic Regression Analysis and Reporting," *The Journal of Educational Research* 96, no. 1 (2002): 3–14.

28. C. Cortes and V. Vapnik, "Support-vector Networks," *Machine learning* 20, no. 3 (1995): 273–297.

29. P. Domingos and M. Pazzani, "On the Optimality of the Simple Bayesian Classifier Under Zero-One Loss," *Machine learning* 29, no. 2 (1997): 103–130.

30. L. Breiman, "Random Forests," *Machine learning* 45, no. 1 (2001): 5–32.

16146840, 2026, 42, Downloaded from https://advanced.onlinelibrary.wiley.com/doi/10.1002/aenm.202505470 by Forschungszentrum Juelich GmbH, Wiley Online Library on [17/11/2026]. See the Terms and Conditions (https://onlinelibrary.wiley.com/terms-and-conditions) on Wiley Online Library for rules of use; OA articles are governed by the applicable Creative Commons License

31. T. Cover and P. Hart, "Nearest Neighbor Pattern Classification," *IEEE Transactions on Information Theory* 13, no. 1 (1967): 21–27.

32. L.-T. Wu, B. J. Hwang, and J.-C. Jiang, "Combined Machine Learning and Computational Protocols to Predict Electrolyte Behavior and SEI Formation in Li-metal Batteries," *Chemical Engineering Journal* 515 (2025): 163801.

33. Y. LeCun, Y. Bengio, and G. Hinton, "Deep Learning," *Nature* 521, no. 7553 (2015): 436–444.

34. M. K. Aydinol, A. F. Kohan, and G. Ceder, "Ab Initio Calculation of the Intercalation Voltage of Lithium-transition-metal Oxide Electrodes for Rechargeable Batteries," *Journal of Power Sources* 68, no. 2 (1997): 664–668.

35. M. Bianchini, J. Wang, R. J. Clément, et al., "The Interplay Between Thermodynamics and Kinetics in the Solid-state Synthesis of Layered Oxides," *Nature Materials* 19, no. 10 (2020): 1088–1095.

36. H.-J. Kim, N. Voronina, K. Köster, et al., "Synergetic impact of dual substitution on anionic–Cationic activity of P2-type sodium manganese oxide," *Energy Storage Materials* 66 (2024): 103224.

37. J. H. Jo, H. J. Kim, N. Yaqoob, et al., "Hollandite-type Potassium Titanium Oxide With Exceptionally Stable Cycling Performance as a New Cathode Material for Potassium-ion Batteries," *Energy Storage Materials* 54 (2023): 680–688.

38. S. V. Stehman, "Selecting and Interpreting Measures of Thematic Classification Accuracy," *Remote Sensing of Environment* 62, no. 1 (1997): 77–89.

39. F. Pedregosa, G. Varoquaux, A. Gramfort, et al., "Scikit-learn: Machine Learning in Python," *Journal of Machine Learning Research* 12, no. 85 (2011): 2825–2830.

40. M. Abadi, P. Barham, J. Chen, et al., "TensorFlow: A system for large-scale machine learning," in *Proceedings of the 12th USENIX conference on Operating Systems Design and Implementation, USENIX Association*, (ACM, 2016), 265–283.

41. X. Glorot, A. Bordes, and Y. Bengio, "Deep Sparse Rectifier Neural Networks" in *Proceedings of the Fourteenth International Conference on Artificial Intelligence and Statistics*, eds. G. Geoffrey, D. David, D. Mirosl (PMLR, 2011), 315–323.

42. S. R. Dubey, S. K. Singh, and B. B. Chaudhuri, "Activation Functions in Deep Learning: A Comprehensive Survey and Benchmark," *Neurocomputing* 503 (2022): 92–108.

43. L. Li, M. Doroslovački, and M. H. Loew, "Approximating the Gradient of Cross-Entropy Loss Function," *IEEE Access* 8 (2020): 111626–111635.

44. K. He, X. Zhang, S. Ren, and J. Sun, "Delving Deep Into Rectifiers: Surpassing Human-Level Performance on ImageNet Classification," in *2015 IEEE International Conference on Computer Vision (ICCV)*, (IEEE, 2015), 1026–1034.

45. S. Ioffe and C. Szegedy, "Batch normalization: Accelerating deep network training by reducing internal covariate shift," in *Proceedings of the 32nd International Conference on International Conference on Machine Learning—Volume 37*, (PMLR, 2015), 448–456.

46. N. Srivastava, G. Hinton, A. Krizhevsky, I. Sutskever, and R. Salakhutdinov, "Dropout: A Simple Way to Prevent Neural Networks From Overfitting," *Journal of Machine Learning Research* 15, no. 1 (2014): 1929–1958.

47. I. Goodfellow, Y. Bengio, and A. Courville, "Deep Feedforward Networks," *Deep Learning* 1 (2016): 161–217.

48. A. Altmann, L. Toloşi, O. Sander, and T. Lengauer, "Permutation Importance: A Corrected Feature Importance Measure," *Bioinformatics* 26, no. 10 (2010): 1340–1347.

49. S. M. Lundberg and S.-I. Lee, "A unified approach to interpreting model predictions," in *Proceedings of the 31st International Conference on Neural Information Processing Systems*, (Curran Associates Inc., 2017), 4768–4777.

50. K. Köster, T. Binninger, and P. Kaghazchi, "Optimization of Coulomb Energies in Gigantic Configurational Spaces of Multi-element Ionic Crystals," *Npj Computational Materials* 11, no. 1 (2025): 202.

51. S. P. Ong, W. D. Richards, A. Jain, et al., "Python Materials Genomics (pymatgen): A Robust, Open-source Python Library for Materials Analysis," *Computational Materials Science* 68 (2013): 314–319.

52. H. B. Callen, *Thermodynamics and an Introduction to Thermostatistics* (John Wiley & Sons, 1993).

53. C. Sutton and S. V. Levchenko, "First-principles Atomistic Thermodynamics and Configurational Entropy," *Frontiers in Chemistry* 8 (2020): 757.

54. G. Kresse and J. Hafner, "Ab Initio Molecular Dynamics for Liquid Metals," *Physical Review B* 47, no. 1 (1993): 558–561.

55. G. Kresse and J. Hafner, "Ab initio molecular-dynamics simulation of the liquid-metal–amorphous-semiconductor transition in germanium," *Physical Review B* 49, no. 20 (1994): 14251–14269.

56. P. E. Blöchl, "Projector Augmented-wave Method," *Physical Review B* 50, no. 24 (1994): 17953–17979.

57. J. P. Perdew, K. Burke, and M. Ernzerhof, "Generalized Gradient Approximation Made Simple," *Physical Review Letters* 77, no. 18 (1996): 3865–3868.

58. K. Köster and P. Kaghazchi, "Hybrid Functionals With Nonempirical Hartree-Fock Parameters for Electronic Structure Calculation of Layered Oxides," *Physical Review B* 109, no. 15 (2024): 155134.

59. V. I. Anisimov, J. Zaanen, and O. K. Andersen, "Band Theory and Mott Insulators: Hubbard U Instead of Stoner I," *Physical Review B* 44, no. 3 (1991): 943–954.

60. A. Togo, L. Chaput, T. Tadano, and I. Tanaka, "Implementation Strategies in Phonopy and phono3py," *Journal of Physics: Condensed Matter* 35, no. 35 (2023): 353001.

61. D. Zagorac, H. Müller, S. Ruehl, J. Zagorac, and S. Rehme, "Recent Developments in the Inorganic Crystal Structure Database: Theoretical Crystal Structure Data and Related Features," *Journal of Applied Crystallography* 52, no. 5 (2019): 918–925.

62. N. Sharma, E. Gonzalo, J. C. Pramudita, et al., "The Unique Structural Evolution of the O3-Phase Na 2/3 Fe 2/3 Mn 1/3 O 2 During High Rate Charge/Discharge: A Sodium-Centred Perspective," *Advanced Functional Materials* 25, no. 31 (2015): 4994–5005.

63. Y. Takahashi, Y. Gotoh, and J. Akimoto, "Single-crystal Growth, Crystal and Electronic Structure of NaCoO2," *Journal of Solid State Chemistry* 172, no. 1 (2003): 22–26.

64. Q. Huang, M. L. Foo, R. A. Pascal, et al., "Coupling Between Electronic and Structural Degrees of Freedom in the Triangular Lattice Conductor NaxCoO2," *Physical Review B* 70, no. 18 (2004): 184110.

65. Y. Gal and Z. Ghahramani, "Dropout as a Bayesian Approximation: Representing Model Uncertainty in Deep Learning" in *Proceedings of The 33rd International Conference on Machine Learning*, eds. B. Maria Florina, Q. W. Kili (PMLR, 2016), 1050–1059.

66. D. A. Anang, J.-H. Park, D. S. Bhange, et al., "O3-type layer-structured Na0.8[Ni1/5Fe1/5Co1/5Mn1/5Ti1/5O3-type layer-structured Na0.8[Ni1/5Fe1/5Co1/5Mn1/5Ti1/5]O2 as long life and high power cathode material for sodium-ion batteries," *Ceramics International* 45, no. 17 (2019): 23164–23171.

67. T. Jin, P.-F. Wang, Q.-C. Wang, et al., "Realizing Complete Solid-Solution Reaction in High Sodium Content P2-Type Cathode for High-Performance Sodium-Ion Batteries," *Angewandte Chemie International Edition* 59, no. 34 (2020): 14511–14516.

68. X.-L. Li, J. Bao, Z. Shadike, et al., "Stabilizing Transition Metal Vacancy Induced Oxygen Redox by Co 2+ /Co 3+ Redox and Sodium-Site Doping for Layered Cathode Materials," *Angewandte Chemie International Edition* 60, no. 40 (2021): 22026–22034.

16146840, 2026, 42, Downloaded from https://advanced.onlinelibrary.wiley.com/doi/10.1002/aenm.202505470 by Forschungszentrum Juelich GmbH, Wiley Online Library on [17/11/2026]. See the Terms and Conditions (https://onlinelibrary.wiley.com/terms-and-conditions) on Wiley Online Library for rules of use; OA articles are governed by the applicable Creative Commons License

69. X. Zhou, C. Yang, X. Liu, et al., "Inhibiting Inter-layer Gliding in Transition Metal Layered Oxides Through Interphase Engineering for Sodium-ion Batteries," *Nature Communications* 16, no. 1 (2025): 6691.

70. J.-X. Guo, Z.-C. Jian, Y.-F. Zhu, et al., "Low-cost Mn-based P2/O3 Heterostructured Layered Oxide Cathodes Based on Orbital-lattice Synergistic Modulation Strategy for Sodium-ion Batteries," *Science China Materials* 68, no. 10 (2025): 3685–3694.

71. P. A. Maughan, A. B. Naden, J. T. S. Irvine, and A. R. Armstrong, "Manipulating O3/P2 Phase Ratio in bi-phasic Sodium Layered Oxides via Ionic Radius Control," *Communications Materials* 4, no. 1 (2023): 6.

72. Y. Zhang, J. Chen, R. Wang, et al., "P2/O3 Biphasic Cathode Material Through Magnesium Substitution for Sodium-Ion Batteries," *ACS Applied Materials & Interfaces* 16, no. 9 (2024): 11349–11360.

73. N. V. Chawla, in *Data Mining and Knowledge Discovery Handbook*, eds. O. Maimon, L. Rokac (Springer US, 2010), 875–886.

74. L.-Y. Kong, J.-Y. Li, H.-X. Liu, et al., "A Universal Interfacial Reconstruction Strategy Based on Converting Residual Alkali for Sodium Layered Oxide Cathodes: Marvelous Air Stability, Reversible Anion Redox, and Practical Full Cell," *Journal of the American Chemical Society* 146, no. 47 (2024): 32317–32332.

75. Y.-F. Liu, H.-X. Liu, Y.-F. Zhu, et al., "Stabilizing Layered Oxide Cathodes Based on Universal Surface Residual Alkali Conversion Chemistry for Rechargeable Secondary Batteries," *Advanced Materials* 37, no. 9 (2025): 2417540.

76. L.-Y. Kong, H.-X. Liu, Y.-F. Zhu, et al., "Layered Oxide Cathodes for Sodium-ion Batteries: Microstructure Design, Local Chemistry and Structural Unit," *Science China Chemistry* 67, no. 1 (2024): 191–213.

77. C. Ma, J. Alvarado, J. Xu, et al., "Exploring Oxygen Activity in the High Energy P2-Type Na0.78Ni0.23Mn0.69O2 Cathode Material for Na-Ion Batteries," *Journal of the American Chemical Society* 139, no. 13 (2017): 4835–4845.

78. A. Massaro, A. B. Muñoz-García, P. P. Prosini, C. Gerbaldi, and M. Pavone, "Unveiling Oxygen Redox Activity in P2-Type NaxNi0.25Mn0.68O2 High-Energy Cathode for Na-Ion Batteries," *ACS Energy Letters* 6, no. 7 (2021): 2470–2480.

79. X. Li, D. Wu, Y.-N. Zhou, L. Liu, X.-Q. Yang, and G. Ceder, "O3-type Na(Mn0.25Fe0.25Co0.25Ni0.25)O2: AQuaternaryyLayereddCathodeeCompoundd forRechargeablee NaIonnBatteriess," *Electrochemistry Communications* 49 (2014): 51–54.

80. M. Aykol and C. Wolverton, "Local Environment Dependent GGA+U Method for Accurate Thermochemistry of Transition Metal Compounds," *Physical Review B* 90, no. 11 (2014): 115105.

Supporting Information

Additional supporting information can be found online in the Supporting Information section.

Supporting file: aenm70518-sup-0001-SuppMat.docx

16146840, 2026, 42, Downloaded from https://advanced.onlinelibrary.wiley.com/doi/10.1002/aenm.202505470 by Forschungszentrum Juelich Gmbh, Wiley Online Library on [17/11/2026]. See the Terms and Conditions (https://onlinelibrary.wiley.com/terms-and-conditions) on Wiley Online Library for rules of use; OA articles are governed by the applicable Creative Commons License